A multi-scale modeling framework for solidification cracking during welding

Liang, Xiaohui; Agarwal, Gautam; Hermans, Marcel; Bos, Cornelis; Richardson, Ian

DOI
10.1016/j.actamat.2024.120530

Publication date
2025

Document Version
Final published version

Published in
Acta Materialia

Citation (APA)
Liang, X., Agarwal, G., Hermans, M., Bos, C., & Richardson, I. (2025). A multi-scale modeling framework for solidification cracking during welding. *Acta Materialia*, *283*, Article 120530. https://doi.org/10.1016/j.actamat.2024.120530

Acta Materialia 283 (2025) 120530

Contents lists available at ScienceDirect

Acta Materialia

journal homepage: www.elsevier.com/locate/actamat

Full length article

A multi-scale modeling framework for solidification cracking during welding

Xiaohui Liang [a,*], Gautam Agarwal [b], Marcel Hermans [a], Cornelis Bos [a,c], Ian Richardson [a,d]

[a] Material Science and Engineering, TU Delft, Mekelweg 2, 2628 CD, Delft, The Netherlands
[b] Departement of Metallurgical and Materials Engineering, IIT Roorkee, 247667, India
[c] Tata Steel, Research & Development, P.O. box 10000, 1970 CA IJmuiden, The Netherlands
[d] IR Welding Consultancy, Berkel en Rodenrijs, The Netherlands

ARTICLE INFO

Keywords:
Solidification cracking
Liquid feeding
Finite element
Cellular automata
Modeling

ABSTRACT

A multi-scale multi-physics modeling framework has been developed to predict solidification cracking susceptibility (SCS) during welding. The framework integrates a thermo-mechanical finite element model to simulate temperature and strain rate profiles during welding, a cellular automata model to simulate the solidified microstructure in the weld pool, and a granular model to calculate the pressure drop in the mushy zone. Verification was achieved by comparing the model's predictions with welding experiments on two steels, demonstrating its capability to accurately capture the effects of process parameters, grain refinement, and alloy composition on SCS. Results indicate that increasing welding velocity, while maintaining a constant power-to-velocity ratio, extends the size of the mushy zone and increases the maximum pressure drop in the mushy zone, leading to higher SCS. Grain refinement decreases separation velocities and the permeability of liquid channels, which increases SCS, but it also raises the coalescence temperature, resulting in an overall reduction in SCS. Alloy composition impacts SCS through thermal diffusivity and segregation. Lower thermal diffusivity or stronger segregation tends to elongate the mushy zone, resulting in an increase in SCS. This framework provides a robust tool for understanding the mechanisms of solidification cracking, optimizing welding parameters to prevent its occurrence, and comparing SCS of different compositions during alloy design.

1. Introduction

Nowadays, advanced high strength steels, which possess high 0.strength and ductility, have been widely employed in the automotive industry to reduce car body weight and thus CO_2 emissions [1]. The high strength and ductility of advanced high strength steels are achieved with high alloying contents; however, some alloying elements may lead to poor weldability. During welding, the detrimental elements may accumulate in the liquid, resulting in the existence of liquid channels at a low temperature. As a result of thermal contraction and solidification shrinkage, interfaces of liquid channels may separate from each other. If the liquid feeding throughout a liquid channel is not enough to compensate for such a separation, cracks form, known as solidification cracking.

Solidification cracking is a complex problem which is associated with multi-physics. The occurrence of solidification cracking during welding is associated with three factors: the driving force to separate liquid channel interfaces, the existence of liquid channels at a low temperature and insufficient liquid feeding. The three factors correspond to different physics and have to be studied at different length scales. The driving force to separate liquid channel interfaces comes from thermo-mechanical interactions between the solidified weld pool and the base material. As the weld pool is usually at the scale of millimeters, the driving force to separate liquid channel interfaces needs to be evaluated at a macroscale. The second and the third factors are related to the micro-segregation and fluid flow within the liquid channel, which needs to be studied at a micro-scale.

Experimental works [2,3] have been performed to study the influence of processing parameters, including power and velocity, on solidification cracking. Slyvinsky et al. [4] reported that increasing the welding velocity v_s with a constant power Q leads to a decrease in SCS for a nickel-base alloy. The decrease in SCS with increasing welding velocity while keeping the power constant was confirmed by Goodwin [5] and Agarwal et al. [6]. This was explained by a smaller thermal strain generated during welding at a faster welding velocity v_s [6]. Conversely, when the welding velocity v_s is increased with a constant Q/v_s ratio, an increase in SCS was reported by Ohshita et al. [7], Shibahara et al. [8], Suyitno et al. [9], Cicală et al. [10] and Goodwin [5]. Nevertheless, it was also found [11] that increasing the welding velocity promotes the transition from a columnar to an

---

* Corresponding author.
E-mail address: x.liang-2@tudelft.nl (X. Liang).

https://doi.org/10.1016/j.actamat.2024.120530
Received 16 July 2024; Received in revised form 30 October 2024; Accepted 31 October 2024

equiaxed structure in the weld pool and thus inhibits solidification cracking in aluminum alloy 6082.

To further understand and avoid solidification cracking, efforts [12–14] have been made to determine the critical strain or strain rate conditions. Gao et al. [12] investigated solidification cracking in laser welded TRIP steel with digital image correlation and finite element modeling and determined that the critical strain for hot cracking lies in the range of 3.2% to 3.6%. Soysal and Kou [13] developed a test to assess the critical deformation rate for solidification cracking. In their test, a stationary sheet is welded to a sheet moving at a varying speed. The critical deformation rate can thus be determined by plotting the crack length against the moving velocity.

Physics-based microscopic models have been developed to predict solidification cracking for liquid channels in a mushy zone. The RDG (Rappaz–Drezet–Gremaud) model [15] and the SCS model developed by Kou [16,17] are widely used to predict SCS of different alloys. The RDG model calculates the pressure drop from the dendrite tip to the coalescence of the liquid channel, assuming that liquid feeding is enough to compensate for the solid deformation. Solidification cracking occurs when the maximum pressure drop is larger than a critical value, from which a critical strain rate can be determined. In Kou's model [16], solidification cracking occurs when the separation velocity of the liquid channel interfaces is larger than the sum of velocity terms from transversal grain growth and liquid feeding. A SCS criterion [16] has been proposed to qualitatively compare the SCS of alloys with different compositions. Based on Scheil–Gulliver solidification calculations, both the RDG model [15] and the Kou's model [16,17] have successfully predicted the SCS peak in Al-Cu alloys containing between 1 wt% and 2 wt% copper. Following Kou's work [16], Soysal [18] employed different solidification models to evaluate SCS of various steel grades and found that the solidification model with back diffusion gives more reasonable SCS predictions than the solidification model without back diffusion. Later, the RDG model [19] and Kou's model [19–21] have been coupled with phase field models, to explicitly simulate the dendrite structure in the mushy zone and provide a more realistic solidification path compared to Scheil–Gulliver calculations. Geng et al. [21] simulated the dendritic microstructure with a phase field model and evaluated the cracking susceptibility of an Al-Mg (4.0 wt%) alloy using Kou's SCS index. It was found that back diffusion reduced the segregation within the liquid channel, leading to a small SCS despite the large freezing temperature range of the considered alloy. With a multi-phase phase field model, Han et al. [19] studied the influence of the grain boundary energy σ_{ss} on the coalescence behavior of the liquid channel and SCS. It was reported that a high σ_{ss} value suppresses the coalescence of the liquid channel and increases SCS. Yang et al. [22] calculated the maximum pressure drop with the RDG model under different alloy compositions and different grain boundary conditions. Their results show that with a quantitative phase field approach, the RDG model is capable of accurately predicting the liquid rupture state associated with solidification cracking. Liang et al. [23] studied the influence of the pulling velocity and the temperature gradient on SCS under directional solidification conditions and found that increasing pulling velocity or decreasing temperature gradient results in an increase in the maximum pressure drop and thus an increase in SCS. Despite the successful applications of the RDG model and of Kou's model in SCS prediction, due to the high computational cost of phase field models, the aforementioned works are limited to a small domain, which is at most at the scale of several hundred micrometers or even smaller. Full-dimensional simulations which include a whole weld pool or mushy zone are still challenging.

Efforts have been made to achieve SCS prediction in a full-dimensional simulation. Sistaninia et al. [24] developed a three-dimensional granular model to simulate the fluid flow within the liquid channel network during casting. By assuming Poiseuille flow and mass balance in each liquid channel, a partial differential equation was derived that describes the evolution of the liquid pressure in the liquid channel network. It was shown that deep in the mushy zone where the permeability is low, the local pressure can be significantly lower than the pressure predicted by averaging techniques [24]. Later, the proposed granular model was combined with a deformation model and a failure model [25]. The failure model assumed that a crack forms when the pressure reaches a critical pressure, which is related to the liquid channel width. The developed model [25] was then validated with a semi-solid tensile test. The simulated stress and shear deformation agreed well with the experimental data. Following the work of Sistaninia et al. [24,25], Rajani and Phillion [26–28] simulated the pressure profiles in the liquid channel networks in the mushy zone of welded component. However, the simulation was performed on a microstructure which was artificially generated with a Voronoi tessellation. The simulation domain was also limited to a small part of the weld pool. Due to the limitations of existing works, a full-dimensional modeling tool capable of evaluating SCS using real microstructures under varying conditions is still not available.

In this work, a multi-scale multi-physics modeling framework is developed aiming to evaluate solidification cracking susceptibility under different welding conditions. This includes three models, which are coupled sequentially. Firstly, a thermomechanical model is used to calculate the profiles of temperature, stress and strain during welding; then, a cellular automata model is employed to simulate the solidification microstructure based on the thermal profiles. The simulated grain boundary structure in the mushy zone is extracted and employed as a liquid channel network. A granular model is then applied to calculate the pressure drop within the liquid channel network. The developed modeling framework is employed to study the influence of the welding velocity and grain refinement on SCS, which is then compared with experimental results. The details of the three different models are described in Section 2. Subsequently, based on welding experiments performed on a TRIP steel, the modeling framework is employed to study the influence of welding velocity on thermomechanical profiles, solidified microstructure and pressure drop in the liquid channel network. Additionally, the influence of grain refinement and alloy composition on SCS are discussed using the modeling framework.

2. Method

2.1. Thermomechanical modeling

The temperature profile T in a welded component Ω is simulated with a finite element (FE) model by solving

$$\rho c_p \frac{\mathrm{d}T}{\mathrm{d}t} = \nabla \cdot (k\nabla T) + Q \qquad \text{in } \Omega, \tag{1}$$

where ρ is the density, c_p the specific heat, t the time, k the thermal conductivity and Q the volumetric heat source, which is given by a truncated-cone Gaussian heat source model [6,12,29],

$$Q = \frac{3\exp(3)\eta P}{(\exp(3)-1)V_{tc}} \exp\left(\frac{-3r^2}{r_0^2}\right), \tag{2}$$

where P is the power and η the efficiency. V_{tc} is the volume of the truncated cone given by

$$V_{tc} = \frac{\pi}{3}(z_e - z_i)(r_e^2 + r_e r_i + r_i^2) \tag{3}$$

where r_e and r_i are the radius of the heat source on the top and the bottom surface and z_e and z_i the z coordinates of the top and the bottom surface, respectively. r is the radial distance of a given point (x, y, z) to the moving heat source center $(x_c, y_c + vt)$ given by

$$r = \sqrt{(x - x_c)^2 + (y - (y_c + vt))^2}. \tag{4}$$

where v is the welding velocity and t the time. The radius of the truncated-cone heat source r_0 varies linearly with z,

$$r_0 = r_i + (r_e - r_i)\frac{z - z_i}{z_e - z_i}. \tag{5}$$

Heat loss through convection and radiation is applied with a Neumann boundary condition,

$$\boldsymbol{n} \cdot \boldsymbol{q} = h_c(T - T_{amb}) + \varepsilon_r \sigma \left(T^4 - T_{amb}^4\right) \qquad \text{on } \partial\Omega, \tag{6}$$

where $\boldsymbol{n}$ is the interface normal on the boundary, h_c the heat transfer coefficient for convective heat loss, T_{amb} the ambient temperature, ε_r the surface emissivity and σ the Stefan–Boltzmann constant. The initial temperature is set to room temperature.

For the mechanical model, the governing equation for the quasi-static analysis is

$$\nabla \cdot \boldsymbol{\sigma} = \mathbf{0}. \tag{7}$$

where $\boldsymbol{\sigma}$ is the stress tensor. Considering geometric nonlinearity, strain tensor $\boldsymbol{\varepsilon}$ is related to the displacement vector $\boldsymbol{u}$ by

$$\boldsymbol{\varepsilon} = \frac{1}{2}\left[(\nabla \boldsymbol{u})^T + \nabla \boldsymbol{u} + (\nabla \boldsymbol{u})^T \nabla \boldsymbol{u}\right]. \tag{8}$$

The strain tensor can be decomposed into three components,

$$\boldsymbol{\varepsilon} = \boldsymbol{\varepsilon}_T + \boldsymbol{\varepsilon}_e + \boldsymbol{\varepsilon}_p, \tag{9}$$

where $\boldsymbol{\varepsilon}_T$, $\boldsymbol{\varepsilon}_e$ and $\boldsymbol{\varepsilon}_p$ are the thermal strain, elastic strain and the plastic strain, respectively. The material is modeled with a linear elasticity and a perfect plasticity without hardening,

$$\boldsymbol{\sigma} = \mathbb{C} : \boldsymbol{\varepsilon}_e, \tag{10}$$

where $\mathbb{C}$ is the fourth-order elasticity tensor. The thermal strain $\boldsymbol{\varepsilon}_T$, as a function of the temperature, is only considered below the liquidus temperature. To include fixed constraint Γ (the left boundary surface of the welded plate), a Dirichlet boundary condition is applied,

$$\boldsymbol{u} = \mathbf{0} \qquad \text{on } \Gamma. \tag{11}$$

The thermomechanical analysis is performed with commercial software COMSOL. Lagrange quadratic elements are employed in the FE simulation. Hexahedral elements with a size of 0.25 mm are employed near the laser path, while coarser elements are used in regions far from the laser path. A thermomechanical simulation takes around 60 h with 20 cores of an Intel E5-2630 CPU.

2.2. Microstructure modeling

The solidification microstructure is simulated with a cellular automata (CA) model, in which the simulation domain has been discretized into cubic cells. Each cell has properties including grain ID, phase status (solid, liquid and interface) and the temperature at the cell center. Each interface cell also has additional properties including growth length l and growth center. Notably, every grain is associated with a crystal orientation. In each time step, the growth length l of every interface cell is updated with

$$\Delta l = \int_{t_1}^{t_2} v_g \mathrm{d}t. \tag{12}$$

Here, t_1 and t_2 are the time at the start and the end of the time step, respectively. The growth velocity v_g is determined based on local undercooling ΔT, using a polynomial fit tailored to the $v_g(\Delta T)$ function predicted by the Kurz–Giovanola–Trivedi model [30].

Solidification is simulated by updating the phase status of CA cells based on transition rules. A liquid cell transforms into an interface cell when it is captured by a neighboring interface cell. To suppress grid anisotropy, the decentered growth algorithm proposed by Gandin and Rappaz [31] is implemented for capturing liquid cells. Each interface cell is associated with a growth envelope, which is an octahedron aligned with the crystal orientation. If the center of a neighboring liquid cell falls into the growth envelope, then this liquid cell is captured and transforms into a new interface cell. The old growth envelope is truncated to form a new growth envelope in the new interface cell. Details of the decentered growth algorithm can be found in [31]. Additionally, an interface cell transforms into a solid cell, if it has no liquid neighbor.

Nucleation is considered with a phenomenological model [32,33]. The distribution function of nucleation density n_n is given with respect to local undercooling ΔT,

$$\frac{\mathrm{d}n_n}{\mathrm{d}\Delta T} = \frac{N_0}{\Delta T_\sigma \sqrt{2\pi}} \exp\left[-\frac{\Delta T - \Delta T_m}{2\Delta T_\sigma^2}\right], \tag{13}$$

where N_0 is the maximum nucleation density, ΔT_m the mean nucleation undercooling and ΔT_σ the standard deviation for the nucleation undercooling.

Here, the temperature profile obtained from the thermomechanical FE model is employed as an input for the solidification CA simulation. With the Lagrange quadratic interpolation, the temperature T at the center (x_c, y_c, z_c) of a CA cell is determined by summing up the product of the shape function N_i and the FE node temperature T_i within the corresponding FE element

$$T = \sum_i T_i N_i(x_c, y_c, z_c). \tag{14}$$

For all the CA simulations presented in this work, a cell size of 5 μm is employed, which is much smaller compared to the element size (0.25 mm) near the laser path in the thermomechanical model. Due to the high computational cost, solidification microstructure is simulated in a representative volume of 3000×6000×1250 $\mu\mathrm{m}^3$. Each CA simulation takes around 1 h with 20 cores of an Intel E5-2630 CPU.

Since the decentered growth algorithm in the CA model does not incorporate the influence of interfacial energy, jagged interfaces may arise at the grain boundaries, which is unfavorable for the subsequent pressure drop calculation. To mitigate this effect, a smoothing procedure is applied to the solidification microstructure. The smoothing procedure follows the physics of grain growth and assesses the curvature at each CA cell along the grain boundaries. Following Nastac [34], the curvature κ of a CA cell can be estimated with

$$\kappa = \frac{1}{\Delta x}\left(1 - 2f_g\right), \tag{15}$$

where Δx is the CA cell size, f_g the volume fraction of the grain in the corresponding Moore neighborhood. The Moore neighborhood refers to a central cell and its 26 surrounding cells, including all adjacent cells in the horizontal, vertical, and diagonal directions across three dimensions. Unlike Nastac's solidification model, the CA cell in this work only belongs to one grain. In this case, an extended Moore neighborhood is employed for the curvature calculation to achieve better accuracy. During the smoothing process, if the curvature κ is larger than a critical value κ_{crit} or if the volume fraction f_g of the corresponding grain in the extended Moore neighborhood is smaller than a critical value $f_{g,crit}$, the considered CA cell then transforms into the grain with the largest volume fraction in the extended Moore neighborhood. This algorithm iterates over multiple cycles to achieve the desired smoothing effects (fraction of cells with $f_g > f_{g,crit}$ is below a user-defined value).

Following grain boundary smoothing, the microstructure in the mushy zone during welding is extracted at a user-defined time point. The mushy zone is determined as the region between two isotherms: the liquidus temperature T_l and the coalescence temperature T_c. The coalescence temperature is defined as the temperature at which the liquid channel coalesces, which can be determined either by a critical solid fraction or a critical liquid channel width. In the works by Rappaz et al. [15] and Rajani and Phillion [28], the coalescence temperature is determined with a critical solid fraction of 0.98. In contrast, Rappaz suggested that [35] that coalescence occurs when the liquid channel width is sufficiently small, at the order of nanometers, relative to the thickness of the solid–liquid interface. In other words, coalescence occurs at a critical channel width, which is at the scale of nanometers when the solid–liquid interfaces are completely flat. If the roughness of the solid–liquid interface is taken into account, coalescence should occur at a much larger liquid channel width than the solid–liquid interface thickness. In this work, the coalescence temperature is determined

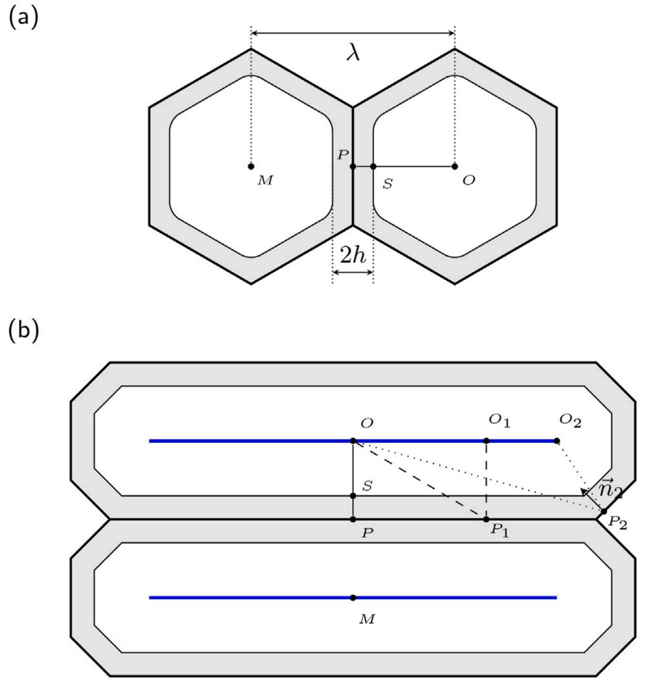

Fig. 1. Illustration of a liquid channel between two columnar grains in different cross sections: (a) perpendicular to the longitudinal axis and (b) parallel to the longitudinal axis. The white regions represent solid, while the gray regions represent liquid. The blue solid lines represent the longitudinal axis of the columnar grains, which passes the grain center and are parallel with the principal direction of the grain. The endpoints of the longitudinal axis are chosen so that their distance to the nearby end of the columnar grain is equal to the mean radial distance of all the grain boundary elements to the grain axis. (For interpretation of the references to color in this figure legend, the reader is referred to the web version of this article.)

using a critical liquid channel width w^c of $0.3\,\mu$m. The corresponding critical solid fraction f_s^c for coalescence is determined with

$$f_s^c = \frac{\frac{4}{3}\pi\left(r - \frac{w^c}{2}\right)^3}{\frac{4}{3}\pi r^3} = \left(1 - \frac{w^c}{2r}\right)^3, \tag{16}$$

where r is the grain radius. It is assumed that the grains exhibit a spherical shape, as equiaxed grains typically form at the center of the weld pool, where solidification cracking is likely to occur. If the grain radius remains constant, the critical liquid channel width corresponds to a consistent critical solid fraction. In this case, the two coalescence criteria (critical solid fraction vs. critical liquid channel width) are effectively equivalent if the grain radius is constant. The impact of these two coalescence criteria will be further discussed in Section 4.

After extraction of the mushy zone, the grain boundary structure is extracted with Dream3D using quick surface meshing and Laplacian smoothing. Subsequently, the extracted grain boundary structure serves as a liquid channel network for the pressure drop calculations.

2.3. Modeling of pressure drop

Following the work of Sistaninia [24,25], assuming Poiseuille flow in the liquid channel, the pressure p evolution in the liquid channel network Ω_l is governed by

$$\frac{2h^3}{3\mu}\nabla^2 p = v_s + v_m \qquad \text{in } \Omega_l, \tag{17}$$

where h is the half width of the liquid channel, μ the viscosity, v_s the separation velocity due to solidification shrinkage and v_m the separation velocity due to mechanical constraints. A Dirichlet boundary condition is applied at the weld pool boundary $\Gamma_{l,D}$ defined by $T = T_l$,

$$p = 0 \qquad \text{on } \Gamma_{l,D}. \tag{18}$$

A Neumann boundary condition is applied on the remaining boundaries $\Gamma_{l,N}$,

$$\boldsymbol{n} \cdot \nabla p = 0 \qquad \text{on } \Gamma_{l,N}. \tag{19}$$

Consider a liquid film between two columnar grains, as shown in Fig. 1. Following Kou's work [16], the radius of a columnar grain is proportional to the square root of the solid fraction $\sqrt{f_s(T)}$. The half width of the liquid channel h can be calculated with

$$h = \frac{\lambda}{2}\left(1 - \sqrt{f_s(T)}\right), \tag{20}$$

where λ is the distance between grain centers or axes, which is calculated by summing up the radius of the two neighboring grains,

$$\lambda = R_t + R_b, \tag{21}$$

where R_t and R_b are the radius of the top grain and bottom grain in Fig. 1b. In practice, grain boundaries are not in perfect cylindrical shapes. The irregular grain boundaries are discretized into triangular elements. For each triangular element, the grain radius is calculated as the distance from the element center to the longitudinal axis of the columnar grain. For example, for an interface element with its center at point P_1, the radius of the top grain is calculated with

$$R_{t,P_1} = \overrightarrow{O_1 P_1} \cdot \boldsymbol{n}_s, \tag{22}$$

where O_1 is the nearest point on the longitudinal axis of the top grain to the considered point P_1 and $\boldsymbol{n}_s$ the unit vector of the considered interface element. The longitudinal axis is determined as a line, which passes the grain center and is parallel with the principal direction of the grain. By approximating both ends of the columnar grains with hemi-spheres, the endpoints of the longitudinal axis are chosen so that their distance to the nearby end of the columnar grain is equal to the mean radial distance of all the interface elements to the grain axis. In this case, the grain radius can be evaluated properly for elements at columnar ends. For example, the radius of the top grain at point P_2 is evaluated with

$$R_{t,P_2} = \overrightarrow{O_2 P_2} \cdot \boldsymbol{n}_s. \tag{23}$$

The separation velocity v_s due to solidification shrinkage is calculated with

$$v_s = \beta\lambda \frac{\mathrm{d}\sqrt{f_s(T)}}{\mathrm{d}T}\dot{T}, \tag{24}$$

where β is the shrinkage factor ($\beta = \rho_s/\rho_l - 1$) and $\dot{T}$ the temperature rate.

The separation velocity v_m due to mechanical constraints is calculated through a direct mapping from the strain field ϵ of the thermomechanical analysis to the mushy zone microstructure. It is also assumed that the deformation only occurs in the liquid. Consider an interface element in the liquid channel with its center at P, as shown in Fig. 1a and 1b. The center of the top columnar grain is O. The line OP intersects the solid–liquid interface at point S. The velocity of point P with respect to point O can be obtained by integrating the strain rate $\dot{\boldsymbol{\epsilon}}$,

$$\boldsymbol{v}_{m,1} = \int_O^P \dot{\boldsymbol{\epsilon}} \cdot \mathrm{d}\boldsymbol{x} = \int_O^P \dot{\boldsymbol{\epsilon}} \cdot \boldsymbol{n}_{OP}\, \mathrm{d}x, \tag{25}$$

where $\boldsymbol{n}_{OP}$ is the unit vector in the direction from O to P. Meanwhile, due to thermal contraction, the length of PS and SO decrease, leading to a contribution $\boldsymbol{v}_{m,2}$ to the separation velocity v_m,

$$\boldsymbol{v}_{m,2} = -\int_S^P \alpha_l \dot{T}\, \mathrm{d}\boldsymbol{x} - \int_O^S \alpha_s \dot{T}\, \mathrm{d}\boldsymbol{x}, \tag{26}$$

where α_l and α_s are the linear thermal expansion coefficient of the liquid and the solid, respectively. Assuming $\alpha_l \approx \alpha_s = \alpha$, $\boldsymbol{v}_{m,2}$ can be written as

$$\boldsymbol{v}_{m,2} = -\int_O^P \alpha\dot{T}\mathrm{d}\boldsymbol{x} = -\int_O^P \alpha\dot{T}\boldsymbol{n}_{OP}\mathrm{d}x. \tag{27}$$

The separation velocity v_m^t due to mechanical constraints from the top columnar dendrite is then given by

$$v_m^t = \boldsymbol{n}_s \cdot \left(\boldsymbol{v}_{m,1} + \boldsymbol{v}_{m,2}\right) = \boldsymbol{n}_s \cdot \int_O^P \left(\dot{\boldsymbol{\varepsilon}} - \alpha \dot{T} \boldsymbol{I}\right) \cdot \boldsymbol{n}_{OP} \mathrm{d}x, \tag{28}$$

where $\boldsymbol{n}_s$ is the interface normal unit vector of the considered interface element and $\boldsymbol{I}$ the identity matrix. Similarly, the separation velocity v_m^b due to mechanical constraints from the bottom columnar dendrite can be obtained and the total mechanical contribution v_m is given by

$$\begin{aligned} v_m &= v_m^t + v_m^b \\ &= \boldsymbol{n}_s \cdot \int_O^P \left(\dot{\boldsymbol{\varepsilon}} - \alpha \dot{T} \boldsymbol{I}\right) \cdot \boldsymbol{n}_{OP} \mathrm{d}x - \boldsymbol{n}_s \cdot \int_M^P \left(\dot{\boldsymbol{\varepsilon}} - \alpha \dot{T} \boldsymbol{I}\right) \cdot \boldsymbol{n}_{MP} \mathrm{d}x, \end{aligned} \tag{29}$$

where $\boldsymbol{n}_{MP}$ is the unit vector in the direction from M to P. $\dot{\boldsymbol{\varepsilon}} - \alpha \dot{T} \boldsymbol{I}$ is the strain rate tensor which needs to be compensated by liquid feeding. In this work, it is called effective strain rate, which in matrix form is written as

$$\dot{\boldsymbol{\varepsilon}} - \alpha \dot{T} \boldsymbol{I} = \begin{bmatrix} \dot{\varepsilon}_{xx} - \alpha \dot{T} & \dot{\varepsilon}_{xy} & \dot{\varepsilon}_{xz} \\ \dot{\varepsilon}_{xy} & \dot{\varepsilon}_{yy} - \alpha \dot{T} & \dot{\varepsilon}_{yz} \\ \dot{\varepsilon}_{xz} & \dot{\varepsilon}_{yz} & \dot{\varepsilon}_{zz} - \alpha \dot{T} \end{bmatrix}. \tag{30}$$

With Eqs. (21), (22), (24) and (29), the total separation velocity v_{tot} at point P is written as

$$\begin{aligned} v_{tot} &= v_s + v_m \\ &= \boldsymbol{n}_s \cdot \left[\beta \frac{\mathrm{d}\sqrt{f_s(T)}}{\mathrm{d}T} \dot{T} \left(\overrightarrow{OP} - \overrightarrow{MP}\right) + \int_O^P \left(\dot{\boldsymbol{\varepsilon}} - \alpha \dot{T} \boldsymbol{I}\right) \cdot \boldsymbol{n}_{OP} \mathrm{d}x \right. \\ &\quad \left. - \int_M^P \left(\dot{\boldsymbol{\varepsilon}} - \alpha \dot{T} \boldsymbol{I}\right) \cdot \boldsymbol{n}_{MP} \mathrm{d}x \right]. \end{aligned} \tag{31}$$

For each triangular element in the liquid channel network, the total separation velocity is calculated. The integration terms in Eq. (31) are evaluated numerically with a Gaussian quadrature rule along the integration path. At quadrature points, the effective strain rate tensor $\dot{\boldsymbol{\varepsilon}} - \alpha \dot{T} \boldsymbol{I}$ is calculated through quadratic Lagrange interpolation based on the profiles of T, $\dot{T}$ and $\dot{\boldsymbol{\varepsilon}}$ from the thermomechanical analysis. The derivative $\mathrm{d}\sqrt{f_s(T)}/\mathrm{d}T$ is determined based on the Scheil–Gulliver calculation from Thermo-Calc. In the Scheil–Gulliver calculation, due to the high diffusivity of carbon in the solid phases, carbon has been set as a fast diffuser. This compensates for the influence of carbon back diffusion on the solidification path, which is an important effect as indicated by Soysal [18]. Back diffusion of substitutional elements are not considered due to their low diffusivities in the solid phases and high cooling rate (at the order of 10^6 K/s) during laser welding.

In this work, Eq. (17) is solved with the finite element method [24, 25]. The weak form formulation is written as

$$\int_\Omega \nabla p \cdot \nabla \varphi \, \mathrm{d}S = -\int_\Omega \frac{3\mu}{2h^3} \left(v_s + v_m\right) \varphi \, \mathrm{d}S + \int_{\Gamma_{l,N}} \varphi \boldsymbol{n} \cdot \nabla p \, \mathrm{d}\Gamma, \tag{32}$$

where φ is the test function. With the Neumann boundary condition defined by Eq. (19), the last term on the right-hand side of Eq. (32) is 0. The weak form formulation can be written into a matrix form [24,25]

$$\mathbf{KP} = \mathbf{F}, \tag{33}$$

with

$$\mathbf{K} = \int_\Omega \mathbf{B}^T \mathbf{B} \, \mathrm{d}S \tag{34}$$

$$\mathbf{F} = -\int_\Omega \frac{3\mu}{2h^3} v_{tot} \mathbf{N} \, \mathrm{d}S. \tag{35}$$

The pressure profile can be obtained by solving the matrix form formulation Eq. (33) for $\mathbf{P}$, which contains pressure values at all finite element nodes on the liquid channel network. The mesh of the liquid channel network comes from quick surface meshing and Laplacian smoothing of Dream3D and contains triangular elements. The size of the elements is similar to the cell size of the CA model (5 μm). The problem is solved with an in-house finite element solver, which is written in C++ and parallelized in a shared memory environment. Each pressure drop calculation takes around 10 min with 20 cores of an Intel E5-2630 CPU. After solving the liquid pressure profile in the mushy zone, the minimum liquid pressure, or equivalently, the maximum pressure drop, is employed to evaluate SCS. A lower minimum pressure or a larger pressure drop indicates a higher SCS and an increased likelihood of solidification cracking.

2.4. Coupling between models

The flow chart of the presented modeling framework is given in Algorithm 1. This modeling framework includes a thermomechanical FE model, a CA solidification model and a granular model. A sequential coupling method is employed to couple the three models. The thermomechanical model calculates the temperature and the displacement profiles during welding. The temperature profile from the thermomechanical analysis serves as input for the CA solidification model which simulates the solidified microstructure in the weld pool. At a user-defined time point, the grain boundary structure in the mushy zone is extracted from the solidified microstructure with Dream3D and then employed as the liquid channel network structure for the granular model, which calculates the pressure profile in the liquid channel network. The profiles of strain rate $\dot{\boldsymbol{\varepsilon}}$ and temperature rate $\dot{T}$ from the thermomechanical analysis also serve as inputs for the pressure drop calculation. With this sequential coupling method, effects like the influence of solidification on temperature profiles or the influence of solid–liquid structure on displacement fields are not considered. This reduces the complexity of the problem and makes the current modeling framework feasible with available computational resources. The limitations of the sequential coupled modeling framework will be discussed in Section 4.

Algorithm 1: The flow chart for the modelling framework.

```
Perform thermal FE simulations to get the temperature $T$ and
  the temperature rate $\dot{T}$;
Perform mechanical FE simulations to get the strain rate $\dot{\varepsilon}$;
Perform CA simulations to get the solidified microstructure;
Smooth the solidified microstructure to remove jagged
  interfaces;
Select a time point $t_s$;
Determine the mushy zone at $t_s$;
Extract the grain boundary structure in the mushy zone with
  Dream3D;
Calculate the pressure profiles in the liquid channel network
  based on the profiles of $T$, $\dot{T}$ and $\dot{\varepsilon}$ at $t_s$;
```

2.5. The experimental conditions

The modeling framework has been employed to simulate the welding experiments performed by Agarwal et al. [29]. Bead-on-plate laser welding experiments were performed on TRIP and DP steel plates at a distance of 5 mm to the free edge, as shown in Fig. 2. The compositions of the TRIP and DP steels are given in Table 1 [29]. Four welding experiments were performed at different welding velocities (10 mm/s, 9 mm/s, 8 mm/s and 7 mm/s) and different powers (1100 W, 990 W, 880 W and 770 W), respectively. In the four experiments, the ratio between the power and the welding velocity was constant. In the TRIP steel samples with welding velocities of 10 mm/s, 9 mm/s and 8 mm/s, longitudinal cracks were observed in the center of the weld, while there was no crack in the TRIP steel sample with a welding velocity of 7 mm/s. Solidification cracks were not observed in DP steel samples. The parameters employed in the simulations can be found in the supplementary material.

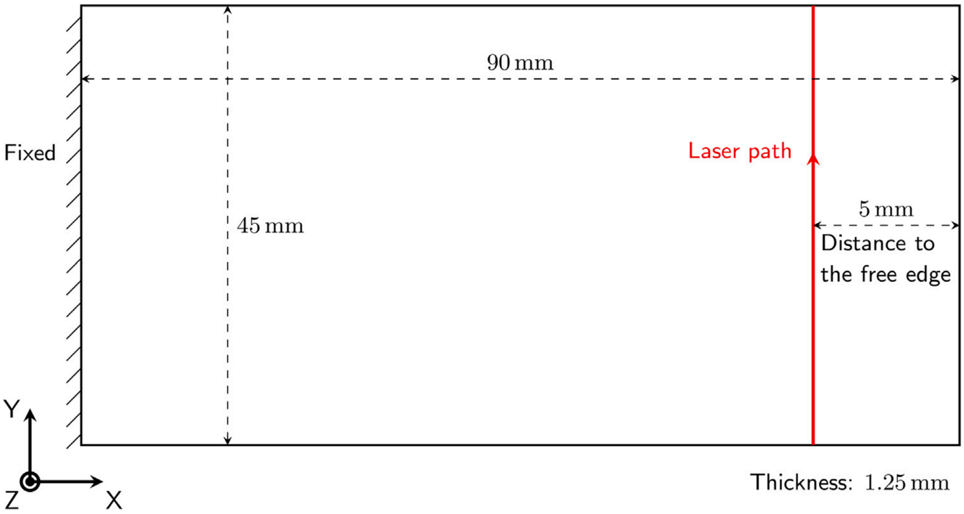

Fig. 2. The experimental configuration in the work of Agarwal et al. [29].

Table 1
Composition of the TRIP and DP steels [29].

Elements (wt%)	C	Mn	Al	Si	Cr	P	S
TRIP	0.19	1.63	1.1	0.35	0.019	0.089	0.005
DP	0.15	2.3	0.03	0.1	0.56	0.01	≈ 0

3. Results

3.1. Profiles of the temperature and the strain rate

With the thermomechanical analysis, the profiles of temperature and strain rate during welding are obtained. The profiles of strain rate components $\dot{\epsilon}_{xx}$, $\dot{\epsilon}_{yy}$ and $\dot{\epsilon}_{zz}$ in the thermomechanical simulation of a TRIP steel sample with a welding velocity of $v = 10\,\mathrm{mm/s}$ at a time when the laser center is at $y = 29\,\mathrm{mm}$, are shown in Fig. 3a, 3c and 3e, respectively. This time point is chosen to ensure that the mushy zone is approximately at half the depth of the plate, minimizing the influence of the front and back edges. As shown in Section 2.3, the separation velocity v_m due to mechanical constraints is related to the effective strain rate $\dot{\epsilon} - \alpha\dot{T}\boldsymbol{I}$. In this case, the components of the effective strain rate are given in Fig. 3b, 3d and 3f. Additionally, isotherms of the liquidus temperature T_l and the coalescence temperature T_c are plotted as red lines; the region between the two red lines is determined as the mushy zone where the liquid is partially solidified. The strain rate profiles in the mushy zone are typical of those associated with solidification cracking. As shown in Fig. 3a, a small zone with positive strain rate $\dot{\epsilon}_{xx}$ is observed near the tail of the weld pool, which is surrounded by a large region with a negative strain rate. When considering the strain rate contribution from thermal contraction, as shown in Fig. 3b, the positive strain rate region near the tail of the weld pool is elongated to the end of the mushy zone, favoring solidification cracking in the welding direction. Similar to the profile of $\dot{\epsilon}_{xx}$, in the profile of $\dot{\epsilon}_{yy}$ (Fig. 3c), a positive strain rate region, which spans over the weld pool tail and part of the mushy zone, is surrounded by a negative strain rate region. When considering the strain rate contribution from thermal contraction, as shown in Fig. 3d, the effective strain rate $(\dot{\epsilon} - \alpha\dot{T}\boldsymbol{I})_{yy}$ is positive in the whole mushy zone, favoring the solidification cracking perpendicular to the welding direction. In the profile of $\dot{\epsilon}_{zz}$ (Fig. 3e), negative strain rate dominates in the mushy zone. When considering the strain rate contribution from thermal contraction, the effective strain rate $(\dot{\epsilon} - \alpha\dot{T}\boldsymbol{I})_{zz}$ in the mushy zone is still negative but with a smaller value (Fig. 3f).

To study the influence of the welding velocity, the results of thermomechanical simulations of TRIP steel samples are compared, as shown in Fig. 4. The length of the weld pool and the length of the mushy zone along the center line are determined based on the temperature profile in each simulation. As shown in Fig. 4b, with increasing welding velocity, both the weld pool length and the mushy zone length increase. With increasing mushy zone length, the liquid feeding in the tail of the mushy zone is more difficult, leading to an increase in SCS.

In the TRIP steel welding experiments, solidification cracks form along the weld path, which is attributed to the strain rate in the x direction; thus, the strain rate component $\dot{\epsilon}_{xx}$ along the center line in the different simulations have been studied. The strain rate profile $\dot{\epsilon}_{xx}$ along the center line in the simulation of the TRIP steel sample with $v = 10\,\mathrm{mm/s}$ is given in Fig. 4c. A strain rate peak is observed at the boundary near the liquidus temperature. As temperature drops in the mushy zone, the solidified material contracts and the strain rate changes from positive to negative. A strain rate valley exists near the coalescence temperature. Following the strain rate valley, due to the interaction between the solidified material and material in the heat affected zone, which undergoes thermal expansion and contraction sequentially, the strain rate along the center line fluctuates and eventually goes back to 0. For comparison, the strain rate profiles $\dot{\epsilon}_{xx}$ in the center of the mushy zone in each simulation are given in Fig. 4d. As the weld pool length in each simulation is different, the strain rate curves are at different locations. With increasing welding velocity, the strain rate curve shifts in the positive direction. As shown in Fig. 4e, as temperature drops from the liquidus temperature to the coalescence temperature, the cooling rate increases. With a larger welding velocity, the cooling rate at the tail of the mushy zone is larger. When the strain rate contribution from thermal contraction is considered, the effective strain rate $(\dot{\epsilon} - \alpha\dot{T}\boldsymbol{I})_{xx}$ is positive in the mushy zone of each simulation, as shown in Fig. 4f. With decreasing temperature, the strain rate $\dot{\epsilon}_{xx}$ decreases while the cooling rate increases, resulting in an earlier valley shape in the curve of $(\dot{\epsilon} - \alpha\dot{T}\boldsymbol{I})_{xx}$. Moreover, the effective strain rate $(\dot{\epsilon} - \alpha\dot{T}\boldsymbol{I})_{xx}$ in the simulation with a larger welding velocity tends to be larger, representing a higher SCS.

3.2. Microstructure

Based on the temperature profile from the thermomechanical analysis, the microstructure in the weld pool is simulated with a 3D CA model with a cell size of 5.0 μm. The simulated and the experimental microstructures on the top plane of the TRIP steel sample with a welding velocity of 10.0 mm/s are presented in Fig. 5a and 5e–5j. To enable a comparison between the simulated and experimental microstructures at the same scale, small regions of the simulated microstructure (C1–C4) are extracted from Fig. 5a. The experimental microstructures are

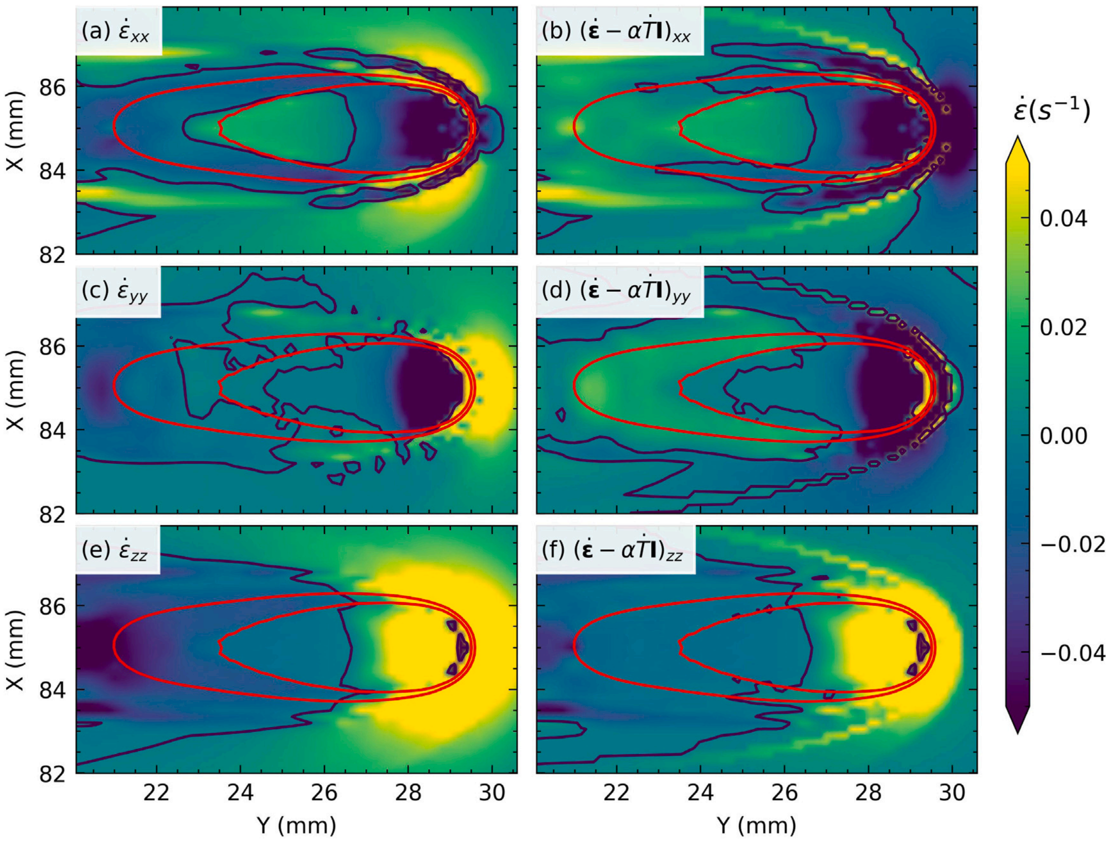

Fig. 3. The strain rate profiles in the TRIP steel welding simulation with $v = 10\,\mathrm{mm/s}$ at the time when the laser center is at $y = 29\,\mathrm{mm}$: (a) $\dot{\varepsilon}_{xx}$, (b) $(\dot{\varepsilon} - \alpha\dot{T}\boldsymbol{I})_{xx}$, (c) $\dot{\varepsilon}_{yy}$, (d) $(\dot{\varepsilon} - \alpha\dot{T}\boldsymbol{I})_{yy}$, (e) $\dot{\varepsilon}_{zz}$ and (f) $(\dot{\varepsilon} - \alpha\dot{T}\boldsymbol{I})_{zz}$. The blue lines represent contour lines for zero strain rate, while the red lines depict isotherms of the liquidus temperature T_l and the coalescence temperature T_c. (For interpretation of the references to color in this figure legend, the reader is referred to the web version of this article.)

obtained by reconstructing prior austenite grains using OIM analysis based on EBSD measurements. The initial microstructure of the simulations is initialized randomly with a Voronoi tessellation. As the laser moves along the welding path, solid grains melt and a weld pool forms. Upon cooling, the grains at the boundary of the weld pool grow epitaxially into the weld pool, competing with each other. The grains with one of their $\langle 100\rangle$ crystallographic directions parallel with the temperature gradient win the competition and form large columnar grains. The simulated columnar grains (Fig. 5h and 5i) agree with the experimental observations (Fig. 5j). As solidification proceeds from the weld pool boundary to the center, the angle between the solid–liquid interface and the welding direction decreases, leading to an increase in the solidification velocity. The increase in the solidification velocity promotes the columnar-to-equiaxed transition (CET) [33]. Small equiaxed grains are observed in both the simulation and the experiment, as shown in Fig. 5e, 5f and 5g.

The welding velocity has an impact on the solidified microstructure, as demonstrated in Fig. 5a–5d and Fig. 6, in which the simulated microstructures on the top plane (Fig. 5) and in the longitudinal (YZ) cross section (Fig. 6) of TRIP steel samples with different welding velocities are presented. In the top plane, the microstructures are dominated by columnar grains growing from weld pool boundary to weld pool center in all the simulations, as shown in Fig. 5a–5d. In the weld pool center, some equiaxed grains are observed, which are formed due to nucleation. With decreasing weld velocity, the number of equiaxed grains along the weld pool centerline decreases and grains nucleated in the weld pool center tend to extend in the welding direction, forming red columnar grains shown in Fig. 5d. In the cross section along the centerline, fine-grained microstructures are observed in all the simulations, as shown in Fig. 6a–6h. Based on the aspect ratio and propagating direction of those grains, three types of grains are identified in the cross-section microstructures: equiaxed grains (aspect ratio ≈ 1), columnar grains (aspect ratio ≫ 1) propagating from weld pool boundary to the weld pool center, columnar grains (aspect ratio ≫ 1) propagating in the welding direction. In the cross section along the weld pool centerline, equiaxed grains are observed in all the simulations. With increasing welding velocity, the solidification velocity in the center of the weld pool increases, which leads to a more significant nucleation and more equiaxed grains in the weld center. This finding is consistent with experimental observations that higher velocities promote CET [11]. In the simulation with the highest velocity $v = 10\,\mathrm{mm/s}$, the cross-section microstructure is dominated by equiaxed grains, while columnar grains propagating from the weld pool boundary to the weld pool center are also observed. At the grain boundaries of those columnar grains in the weld pool center, the separation velocity of liquid channels is high, which increases the chance of solidification cracking. In simulations with relatively low welding velocities ($v = 8.0\,\mathrm{mm/s}$ and $v = 7.0\,\mathrm{mm/s}$), columnar grains propagating in the welding direction are observed in the weld center, as shown in Fig. 6e–6h. Those grains are formed due to the elliptical weld pool shape and the low fraction of equiaxed grains. This supports the experimental observation from Agarwal et al. [29], in which grains bend towards the weld center. It has been reported [36] that grain refinement helps to prevent solidification cracking. In the work of Schempp et al. [11], the grain refinement effect introduced by CET successfully inhibits solidification cracking. In general, a finer microstructure reduces the separation velocity exerted on each liquid channel, leading to a decrease in solidification cracking susceptibility. In the current case, the fraction of the equiaxed grains increases with increasing welding velocity. However, the fraction of the equiaxed grains is still very small, which is not enough to prevent solidification cracking.

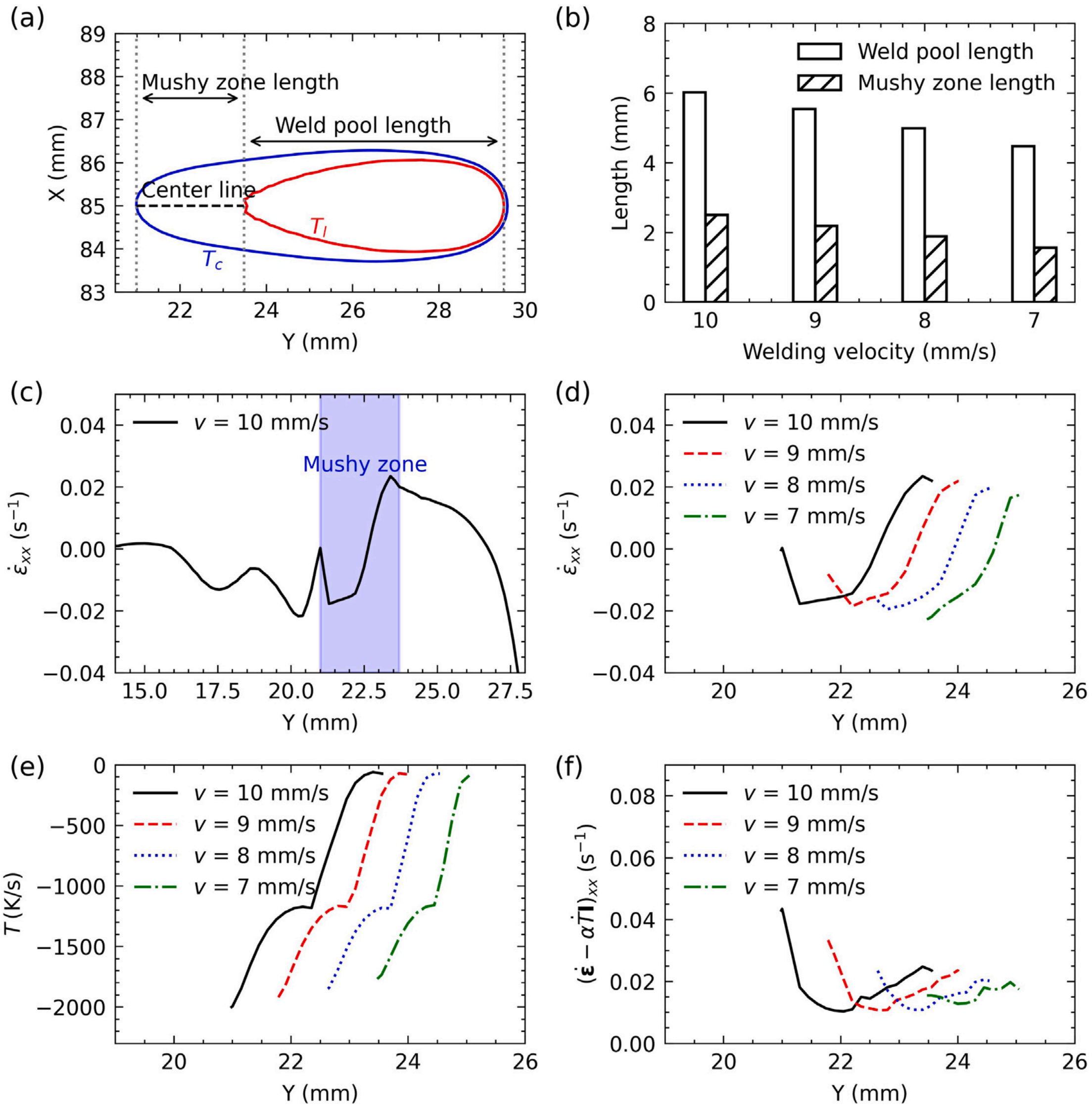

Fig. 4. The influence of the welding velocity on thermomechanical profiles along the center line of the weld. (a) The shape of the melt pool and mushy zone at the time when the laser center is at $y = 29\,\mathrm{mm}$. The length of the mushy zone and the weld pool are determined along the center line. (b) Increasing weld velocity elongates the weld pool and the mushy zone, (c) The strain rate component $\dot{\varepsilon}_{xx}$ along the center line in the simulation with a welding velocity of $10\,\mathrm{mm/s}$. (d) The influence of the welding velocity on strain rate component $\dot{\varepsilon}_{xx}$ along the center line. (e) The influence of the welding velocity on the temperature rate $\dot{T}$ along the center line. (f) The influence of the welding velocity on the effective strain rate component $(\dot{\varepsilon} - \alpha\dot{T}\boldsymbol{I})_{xx}$ along the center line.

3.3. Pressure drop in the mushy zone

The pressure drop in the liquid channel can be obtained by solving Eq. (17) based on the temperature profile, strain rate profile and the microstructure. In each simulation, the pressure drop calculation is performed at the time when the laser center is at $y = 29\,\mathrm{mm}$. Here, the liquid channel network is generated based on the simulated microstructures using a coalescence temperature of $1554\,\mathrm{K}$, corresponding to a critical solid fraction of 0.989. This critical solid fraction is determined with a critical liquid channel width of $0.3\,\mu\mathrm{m}$ and a grain size of $42.5\,\mu\mathrm{m}$. As the grain size does not differ significantly across the simulations, the same coalescence temperature is applied for all the simulations with different welding velocities. The simulated profiles of pressure p, grain distance λ and separation velocities due to solidification shrinkage v_s and mechanical constraints v_m on the top plane in the pressure drop calculation with $v = 10\,\mathrm{mm/s}$ are given in Fig. 7a–7d. In the pressure drop calculation, the grain distance λ is estimated based on the simulated microstructure. As shown in Fig. 7b, the grain distance near the weld pool boundary is small due to the growth competition between the grains with different orientations. As solidification proceeds, grains with favorable orientations win the competition and grow into large columnar grains, leading to an increase in the grain distance λ. In the weld pool center, some small values of grain distance λ are observed due to the appearance of equiaxed grains. Based on the estimated grain distance for each liquid channel element, the half width of the liquid channel h and the separation velocities due to solidification shrinkage v_s and mechanical constraints v_m can be calculated. As shown in Fig. 7c, the separation velocity v_s due to solidification shrinkage is large in the region near the liquidus isotherm, where v_s is small in the region near the coalescence isotherm. This is because the separation velocity due to solidification shrinkage v_s is proportional to $\mathrm{d}\sqrt{f_s(T)}/\mathrm{d}T$, which is large in the initial stage of solidification and small in the final stage, as indicated by the Scheil–Gulliver solidification curve. Unlike v_s, which depends on the solidification stage, the separation velocity due to mechanical constraints v_m depends on the effective strain rate and the grain distance λ. The separation velocity v_s is large at grain boundaries with large λ values, especially in the center of the weld pool, where the long columnar grains contact equiaxed grains or columnar grains growing from the opposite weld pool boundary, as shown in Fig. 7d.

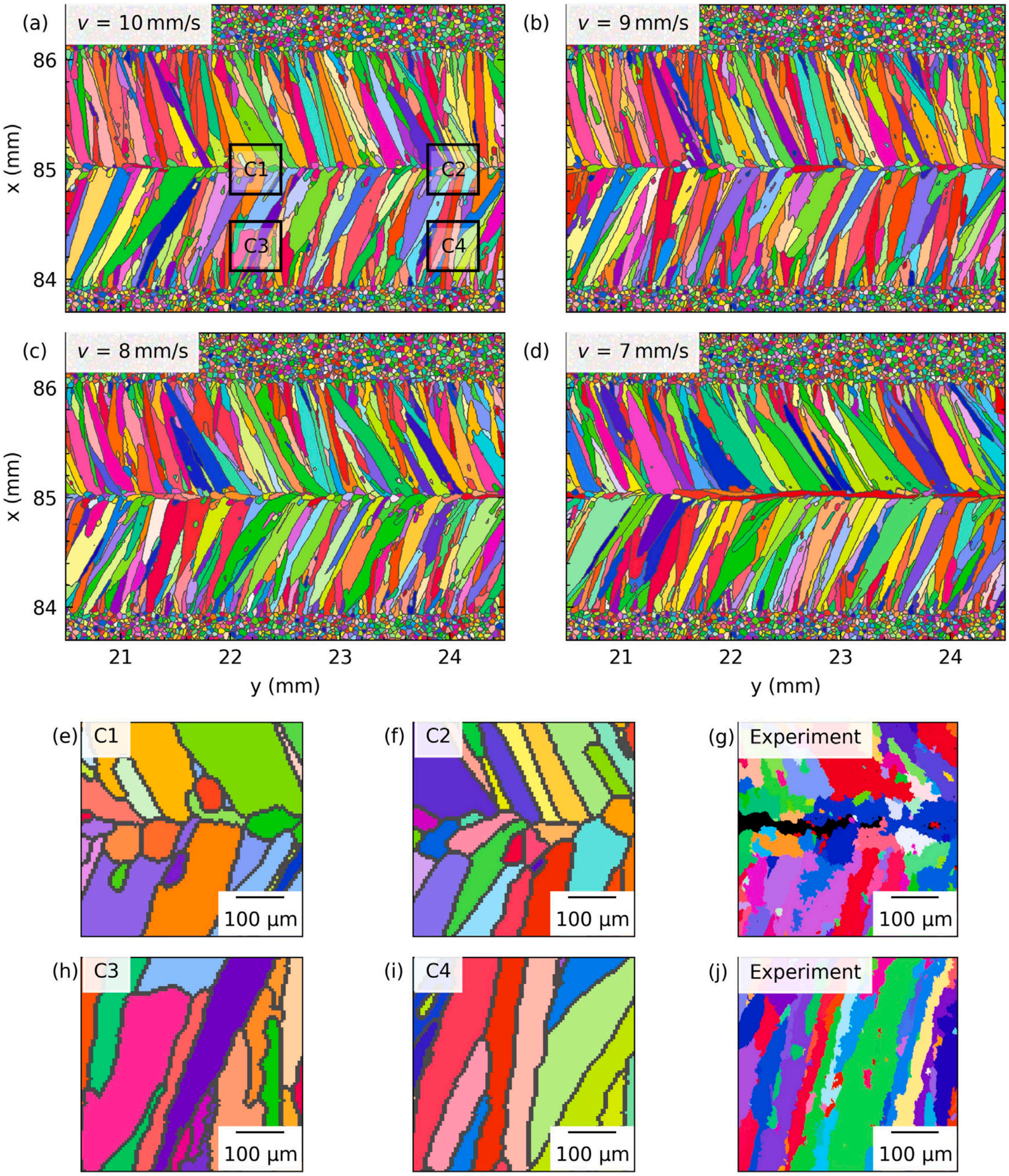

Fig. 5. The simulated microstructure in the top plane (plane-XY) of the TRIP steel samples with different welding velocities: (a) $v = 10\,\mathrm{mm/s}$, (b) $v = 9\,\mathrm{mm/s}$, (c) $v = 8\,\mathrm{mm/s}$ and (d) $v = 7\,\mathrm{mm/s}$. To compare the simulated microstructure with the experimental results at the same scale, small regions (C1-C4) are extracted from (a). (e, f) Simulated microstructure in the center of the weld pool (C1 and C2 in (a)). (g) Experimental microstructure in the center of the weld pool. (h, i) Simulated microstructure in the columnar-grained region (C3 and C4 in (a)). (j) Experimental microstructure in the columnar-grained region. The experimental microstructures are obtained by reconstructing prior austenite grains using OIM analysis based on EBSD measurements. All figures are colored with IPF color with respect to the welding (horizontal) direction. The simulated microstructures show good agreements with the experimental observations. (For interpretation of the references to color in this figure legend, the reader is referred to the web version of this article.)

With the profiles of the half width of the liquid channel h and the separation velocities (v_s and v_m), the pressure profile is obtained by solving Eq. (17), as shown in Fig. 7a. At the weld pool boundary defined by the liquidus isotherm, a Dirichlet boundary condition is applied, where the pressure is set to zero. To compensate for liquid channel separation introduced by solidification shrinkage and mechanical constraints, liquid melt flows into liquid channels, causing a pressure drop in the liquid channel network. The pressure drop is faster parallel to the welding direction than perpendicular to the welding direction. In this case, the lowest pressure is observed at the tail of the mushy zone, which is consistent with the fact that solidification cracking occurs in the center of the weld in experiments.

A 3D view of the pressure profiles in the simulations with different welding velocities is presented in Fig. 7e–7h. For each simulation, a minimum pressure is found in the center of the mushy zone tail. With increasing welding velocity, the absolute value of the minimum pressure increases, indicating an increase in SCS. According to Agarwal et al. [6], solidification cracking occurs in the experiments with $v = 10\,\mathrm{mm/s}$, $v = 9\,\mathrm{mm/s}$ and $v = 8\,\mathrm{mm/s}$, while no solidification crack is observed in the experiment with $v = 7\,\mathrm{mm/s}$. Thus, the simulation results agree well with the experimental observations. The observation that increasing welding velocity increases solidification cracking susceptibility is also confirmed in other experimental works [7,37,38].

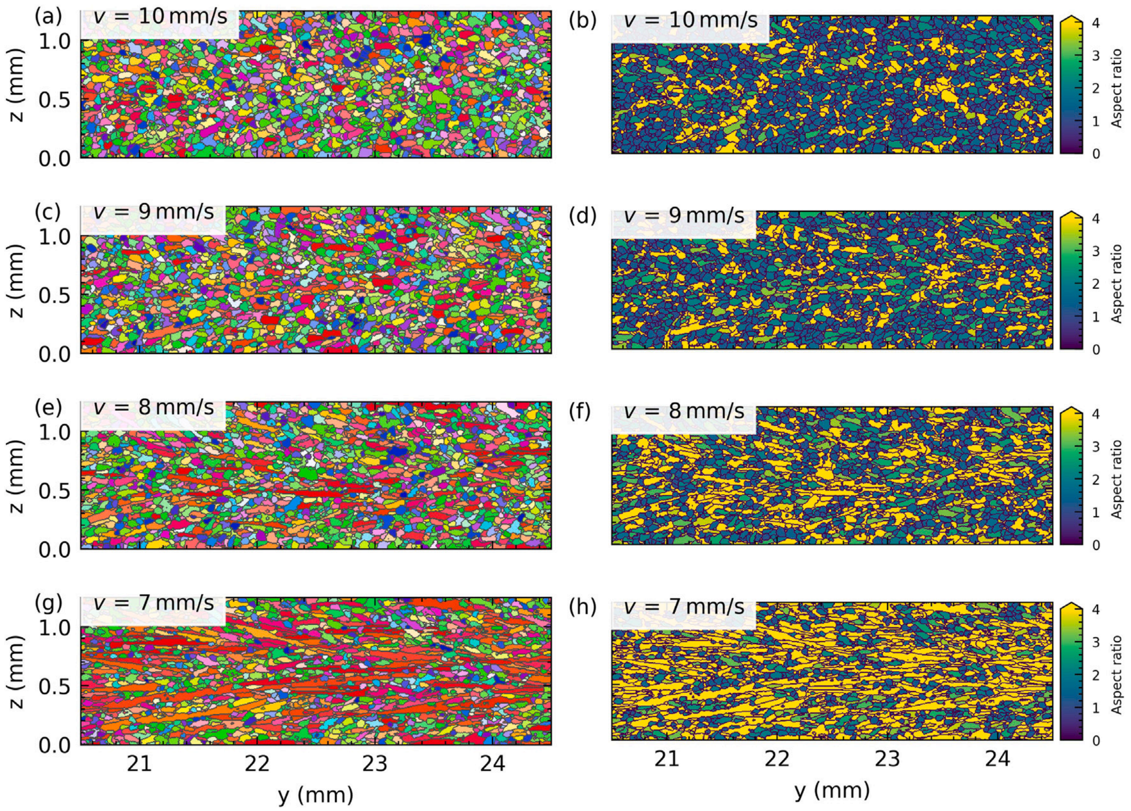

Fig. 6. The simulated microstructure in the cross section (plane-YZ at the weld centerline) of the TRIP steel samples with different welding velocities: (a, (b) $v = 10\,\mathrm{mm/s}$, (c, (d) $v = 9\,\mathrm{mm/s}$, (e, (f) $v = 8\,\mathrm{mm/s}$ and (g, (h) $v = 7\,\mathrm{mm/s}$. In a, c, e, g, grains are colored with IPF color with respect to Y direction, whereas in b, d, f, h, grains are colored based on their aspect ratio. With increasing welding velocity, the volume fraction of equiaxed grains (aspect ratio ≈ 1) in the center of the weld pool increases. Two kinds of columnar grains (aspect ratio $\gg 1$) are observed in the simulated microstructures: columnar grains propagating in the direction perpendicular to the welding direction (b), columnar grains propagating in the welding direction (f, h). (For interpretation of the references to color in this figure legend, the reader is referred to the web version of this article.)

As demonstrated in the experiments (centerline cracks) and simulations (minimum pressure in the mushy zone tail), the centerline region is identified as the most critical region for cracking. In this context, a section along the centerline has been extracted from the simulations, and key variables including pressure p, solid fraction f_s and separation velocities due to mechanical constraints v_m and solidification shrinkage v_s have been averaged and plotted with respect to the y axis (welding direction), as shown in Fig. 8. As shown in Fig. 8a and 8b, starting from the weld pool boundary in the negative y direction, the averaged solid fraction f_s increases while the averaged liquid pressure p drops continuously from 0. Note that the weld pool boundary in the plane-YZ along the centerline is not a vertical line perpendicular to the y axis but rather a "C"-shaped curve. The curvature of the weld pool boundary leads to an artificial plateau in the initial solidification stage of the averaged pressure curves in Fig. 8a. Excluding this artificial plateau, the averaged pressure initially drops rapidly in the negative y-direction, indicating a significant fluid flux from the weld pool into the liquid channels within the mushy zone. As solidification proceeds, the slope of the pressure curves gradually decreases, eventually reaching zero at the point of coalescence. The gradual change in the slope of the pressure curves demonstrates that the fluid flux is progressively consumed to compensate for the separation of liquid channels caused by solidification shrinkage and mechanical constraints. The final slope value of zero aligns with the Neumann boundary condition, where the pressure gradient equals zero at boundaries in contact with solid regions. With increasing welding velocity, the minimum pressure decreases, which agrees with the findings from the 3D view. The averaged separation velocities due to mechanical constraints v_m and solidification shrinkage v_s are given in Fig. 8c and 8d. The averaged separation velocity due to mechanical constraints v_m fluctuates around $1 \sim 2$ μm/s in the mushy zone, while the averaged separation velocity due to solidification shrinkage v_s decreases from a large value of approximately 30 μm/s to nearly zero along the negative y direction. The fluctuations in the v_m curves are attributed to variations in grain size and the normal directions of the grain boundary elements. The behavior of v_s agrees with the fact that $\mathrm{d}\sqrt{f_s}/\mathrm{d}T$ decreases as solidification proceeds in Scheil–Gulliver solidification calculations, which also aligns with the results in [28]. In the averaged v_s curves, a sharp transition is observed during the initial solidification stage. This is caused by the sudden change in the shrinkage factor β when the peri-eutectic reaction occurs and the solid phase changes from ferrite to austenite.

4. Discussion

In the results section, the effects of increasing welding velocity while keeping the ratio between the power and the welding velocity constant (i.e., the heat input per unit length) have been studied within the current multi-scale multi-physics framework. With increasing welding velocity, as a result of the increased mushy zone length, increased cooling rate and increased effective strain rate $(\dot{\varepsilon} - \alpha\dot{T}\boldsymbol{I})_{xx}$, the maximum pressure drop in the liquid channel network becomes larger, indicating a higher chance of solidification cracking. The finding from the simulations agrees with the experimental work [6,7,37,38]. In this section, the influences of grain refinement and alloy composition on solidification cracking are studied with the current multi-scale multi-physics framework.

4.1. Influence of grain refinement on solidification cracking

Grain refinement has proved to be an effective method to prevent solidification cracking. In the work of Schempp et al. [11], the grain

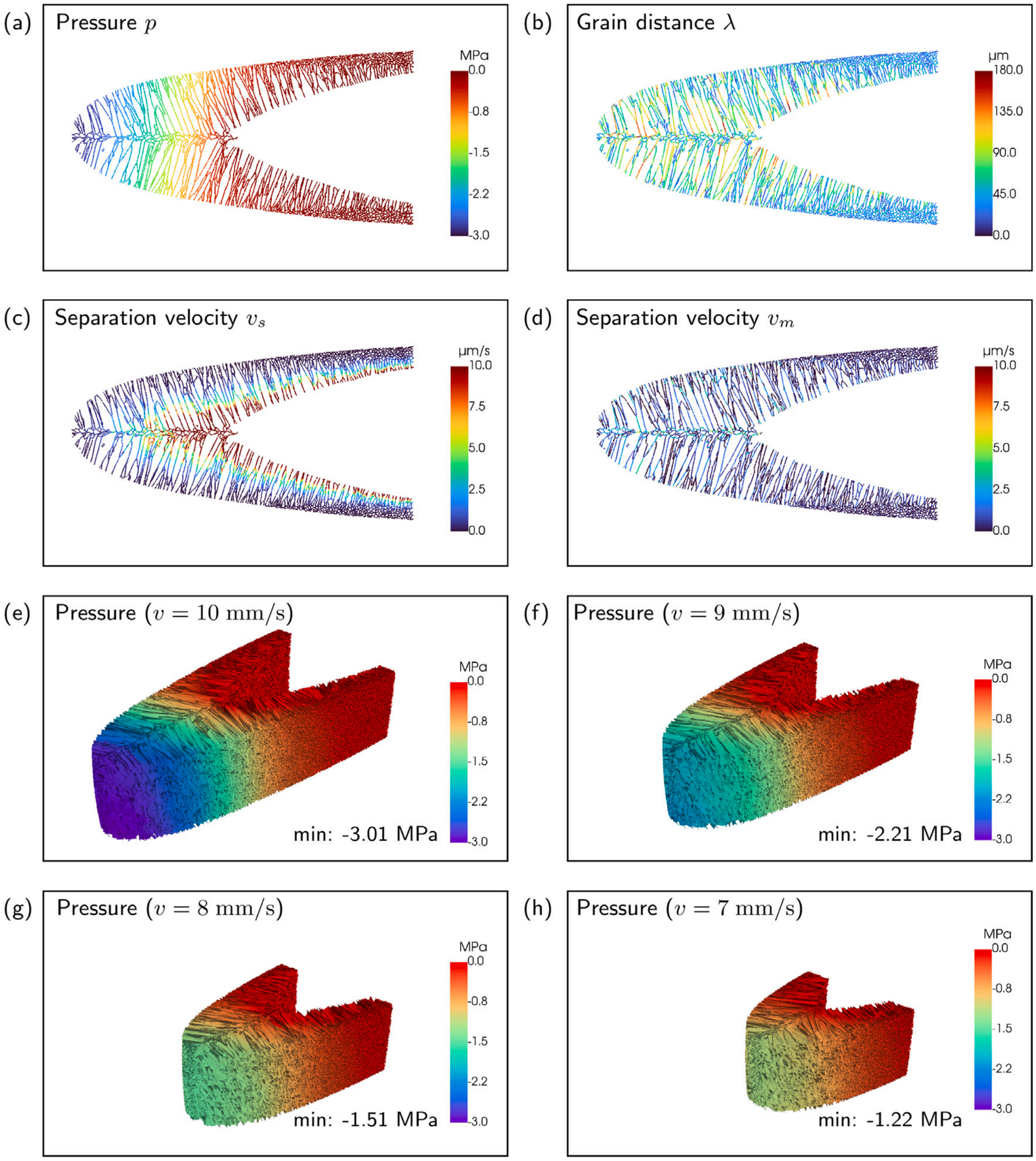

Fig. 7. The profiles of different variables in the top plane in the pressure drop calculation with $v = 10\,\mathrm{mm/s}$: (a) pressure, (b) grain distance λ, (c) separation velocity due to solidification shrinkage v_s and (d) separation velocity due to mechanical constraints v_m. The 3D pressure profiles in the liquid channel network in the simulations with different welding velocities: (e) $v = 10\,\mathrm{mm/s}$, (f) $v = 9\,\mathrm{mm/s}$, (g) $v = 8\,\mathrm{mm/s}$ and (h) $v = 7\,\mathrm{mm/s}$. With decreasing welding velocity, the absolute value of the minimum pressure in the liquid channel network decreases, indicating a decrease in solidification cracking susceptibility. (For interpretation of the references to color in this figure legend, the reader is referred to the web version of this article.)

refinement introduced by a columnar-to-equiaxed transition when increasing the welding velocity inhibits solidification cracking. Opprecht et al. [36] employed yttrium stabilized zirconia as a grain refiner and successfully eliminated solidification cracking in aluminum alloys manufactured by laser beam melting.

The current modeling framework has been employed to investigate the influence of grain refinement on SCS. To mimic the grain refinement effect, the nucleation density N_0 has been artificially increased from $1 \times 10^{13}\,\mathrm{m}^{-3}$ to $5 \times 10^{13}\,\mathrm{m}^{-3}$, $1 \times 10^{14}\,\mathrm{m}^{-3}$ and $5 \times 10^{14}\,\mathrm{m}^{-3}$ for microstructure simulation with a welding velocity of $10\,\mathrm{mm/s}$. With increasing nucleation density, the fraction of equiaxed grains in the center of the weld pool increases, and the grain size decreases, as shown in Figs. 9 and 10a. Here, the coalescence temperature is determined with a critical liquid channel width of $0.3\,\mu\mathrm{m}$ with Eq. (16). A reduction in grain size leads to a corresponding decrease in the critical solid fraction, resulting in an increase in the coalescence temperature, as shown in Fig. 10b. Consequently, with grain refinement, the length of the mushy zone decreases, which leads to a smaller pressure drop and, therefore, a reduction in SCS, as shown in Fig. 10c. The predicted grain refinement effect on SCS agrees with experimental observations [11,36].

To evaluate the influence of coalescence criterion, pressure drop calculations are re-performed by using a critical solid fraction of 0.98 as the criterion to determine the coalescence temperature. In this case, a constant coalescence temperature is applied. As shown in Fig. 10d, with decreasing grain size, the maximum pressure drop increases, indicating a rise in SCS. The increase in the maximum pressure drop is attributed to the combined effects of grain size on the separation velocities and the permeability of the liquid channels, as described by Eq. (17). The

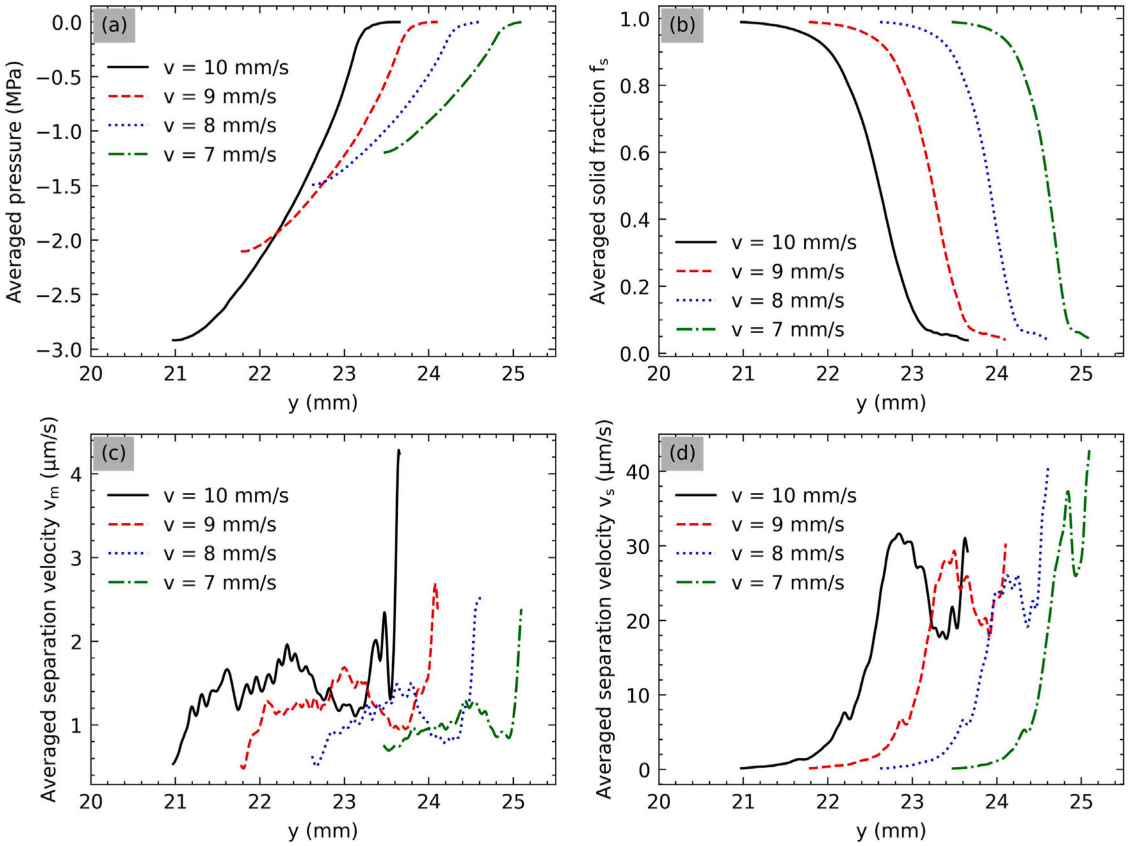

Fig. 8. The profiles of averaged variables in the mushy zone along the weld centerline: (a) the averaged pressure p, (b) the averaged solid fraction f_s, (c) the averaged separation velocity v_s due to solidification shrinkage and (d) the averaged separation velocity v_m due to mechanical constraints.

separation velocities (v_s and v_m) are linearly dependent on grain size, while the permeability ($2h^3/3$) is proportional to r^3, making $\nabla^2 p$ proportional to $1/r^2$. Therefore, as grain size decreases, both the separation velocities and the permeability decrease, resulting in a higher pressure drop and thus an increase in SCS. In this case, using a critical solid fraction as the coalescence criterion leads to grain size effects on SCS that are inconsistent with experimental findings [11,36].

In summary, grain refinement has three key effects: as grain size decreases, the separation velocities decrease, the permeability of liquid channels decreases, and the coalescence temperature increases. The combined effects result in a reduction in SCS, as observed experimentally [11,36]. The first two mechanisms are effectively captured by Eq. (17), while the third mechanism (coalescence temperature variation) can be modeled by using a critical liquid channel width as the coalescence criterion. Under this approach, the proposed model framework accurately predicts the influence of grain refinement on SCS.

4.2. Influence of alloy composition on solidification cracking

Alloy composition has a large impact on the material properties, and consequently, SCS. Here, the influence of alloy composition on SCS is examined by comparing TRIP steel and DP steel. As indicated in [29], the TRIP steel is susceptible to solidification cracking, while the DP steel is not. These differences in SCS behavior are attributed to variations in alloy composition, which lead to differences in thermal diffusivity and coalescence temperature. As illustrated in Fig. 11a, the thermal diffusivity of TRIP steel is generally lower than that of the DP steel across most of the temperature range of interest. This results in a slower heat loss and consequently a longer melt pool in the TRIP steel sample, as shown in Fig. 11c. The melt pool tail in the TRIP steel sample is sharper compared to that in the DP steel sample. In addition, different alloy compositions result in different segregation behaviors. Fig. 11b presents Scheil–Gulliver solidification curves calculated with Thermo-Calc, indicating similar liquidus temperatures for both steels. However, due to the presence of alloying elements such as sulfur and phosphorus, the TRIP steel exhibits a more pronounced segregation behavior and has a lower coalescence temperature compared to the DP steel. The coalescence temperature for the TRIP steel is around 1554 K, while the coalescence temperature for the DP steel is around 1700 K. Consequently, the freezing temperature range of the TRIP steel is larger than that of the DP steel. As a combined effect of the lower thermal diffusivity and the larger freezing temperature range in the TRIP steel, the mushy zone in the TRIP steel sample is longer than that in the DP steel sample at the same welding velocity 10 mm/s, as shown in Fig. 11c. Note the contribution from the lower thermal diffusivity is not negligible, as the mushy zone in the TRIP steel sample is still longer than that of the DP steel sample even when employing the same coalescence temperature (1700 K), as shown in Fig. 11c.

The difference in the melt pool shape of the TRIP steel sample and the DP steel sample results in distinct solidified microstructures, as shown in Fig. 11d and 11e. In the TRIP steel sample, long columnar grains grow from weld pool boundary towards the centerline of the weld pool and some equiaxed grains are observed in the weld pool center. In the DP steel sample, columnar grains growing from weld pool boundary to weld pool center are also identified. However, compared to the TRIP steel sample, the columnar grains in the DP steel sample propagate at a smaller angle relative to the welding direction. Additionally, some long columnar grains with one of their ⟨100⟩ crystallographic directions parallel with the welding direction appear in the center of the weld pool. The difference in solidified microstructure leads to different strain partitioning, thus influencing SCS.

SCS of the two different steels are quantified using pressure drop calculations in the liquid channel network. The calculated liquid pressure in the liquid channel network is given in Fig. 11f and 11g. At

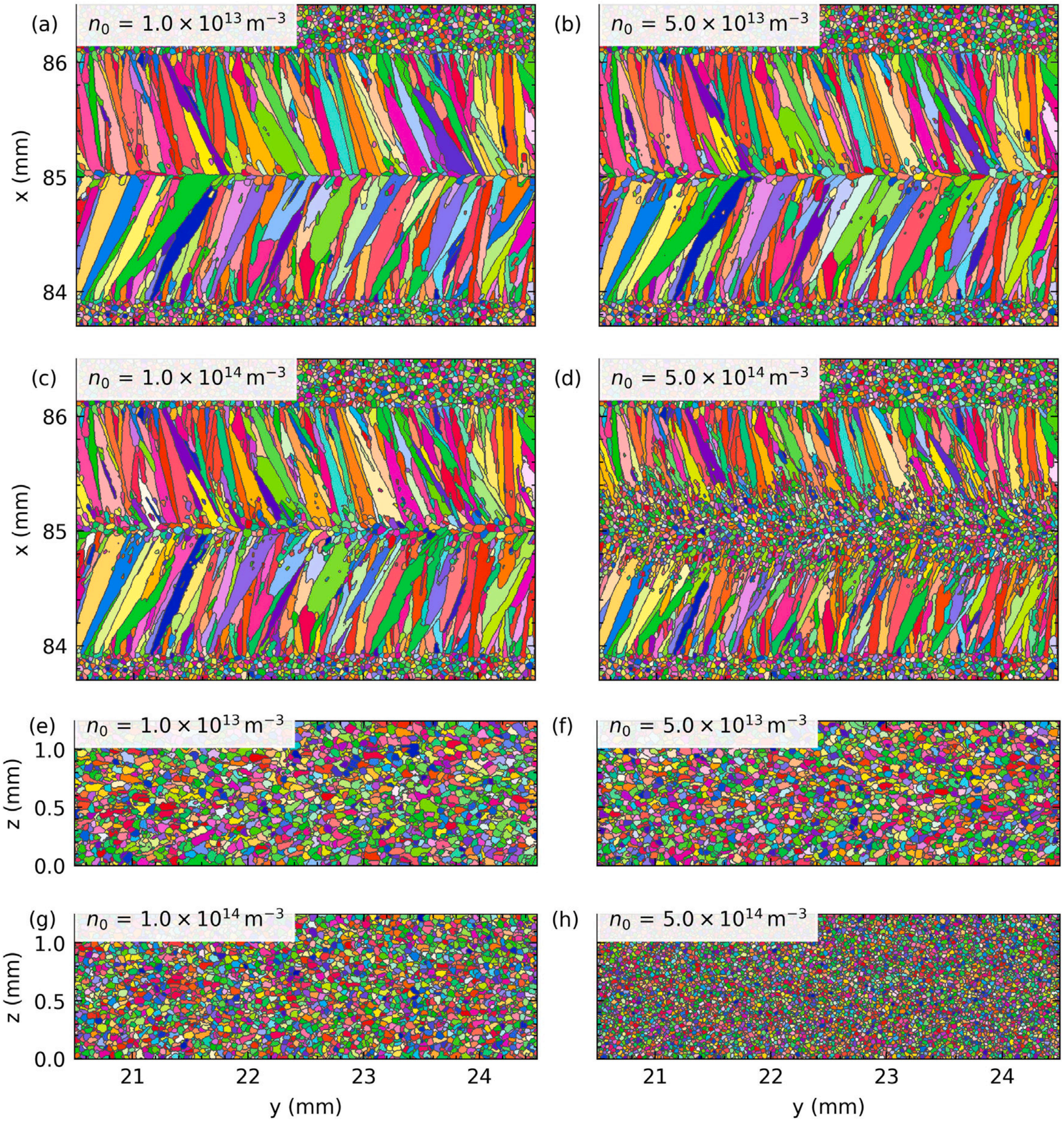

Fig. 9. The simulated microstructure in the top plane (plane-XY) and the cross section (plane-YZ) of a TRIP steel sample with different nucleation densities N_0: (a, (e) $1 \times 10^{13}\,\mathrm{m}^{-3}$, (b, (f) $5 \times 10^{13}\,\mathrm{m}^{-3}$, (c, (g) $1 \times 10^{14}\,\mathrm{m}^{-3}$ and (d, (h) $5 \times 10^{14}\,\mathrm{m}^{-3}$. Grains are colored with IPF color with respect to Y direction. With increasing nucleation density n_0, the columnar-to-equiaxed transition occurs earlier and the grain size of the equiaxed grains decreases. (For interpretation of the references to color in this figure legend, the reader is referred to the web version of this article.)

the same welding velocity $10\,\mathrm{mm/s}$, the absolute value of the minimum pressure in the DP steel sample is $0.12\,\mathrm{MPa}$, which is much lower than the $3.01\,\mathrm{MPa}$ in the TRIP steel sample. This finding aligns with the experimental observation [29] that the DP steel is not susceptible to solidification cracking.

In summary, the studied TRIP steel exhibits higher SCS than the DP steel, which is attributed to its lower thermal diffusivity and larger freezing temperature range. TRIP steels typically contain alloying elements such as aluminum and silicon to stabilize austenite and promote the transformation-induced plasticity (TRIP) effect. However, the addition of aluminum and silicon significantly decreases thermal conductivity and thermal diffusivity (refer to the supplementary material), thereby extending the mushy zone and increasing SCS. Furthermore, the presence of alloying elements like phosphorus and sulfur in TRIP steel lowers the coalescence temperature and enlarges the freezing temperature range, which further increase SCS. It should be noted that the phosphorus content in most commercial TRIP steels is lower than that in the studied TRIP steel. To check this effect, the composition of the TRIP steel is modified by removing sulfur and decreasing phosphorus content to 0.01%, matching the composition of the DP steel. This modified composition is referred to as modified TRIP steel. As shown in Fig. 11b, the freezing temperature range of the modified TRIP steel is smaller than the original TRIP steel but larger than the DP steel, indicating that the modified TRIP steel still has higher SCS than the DP steel.

Compared to traditional models [12,21,22,29], which studied solidification cracking either at the macro or micro scale, the current multi-scale multi-physics modeling framework integrates various physical mechanisms across different scales and captures the influence of parameters such as welding velocity and alloy composition on solidification cracking susceptibility, showing strong agreement with experimental observations. Moreover, the integration of a cellular automata solidification model generates physically realistic microstructures, enabling a quantitative explanation of grain refinement effects on solidification cracking, which has never been achieved before [15,28]. The comprehensiveness of this approach represents a significant advancement in

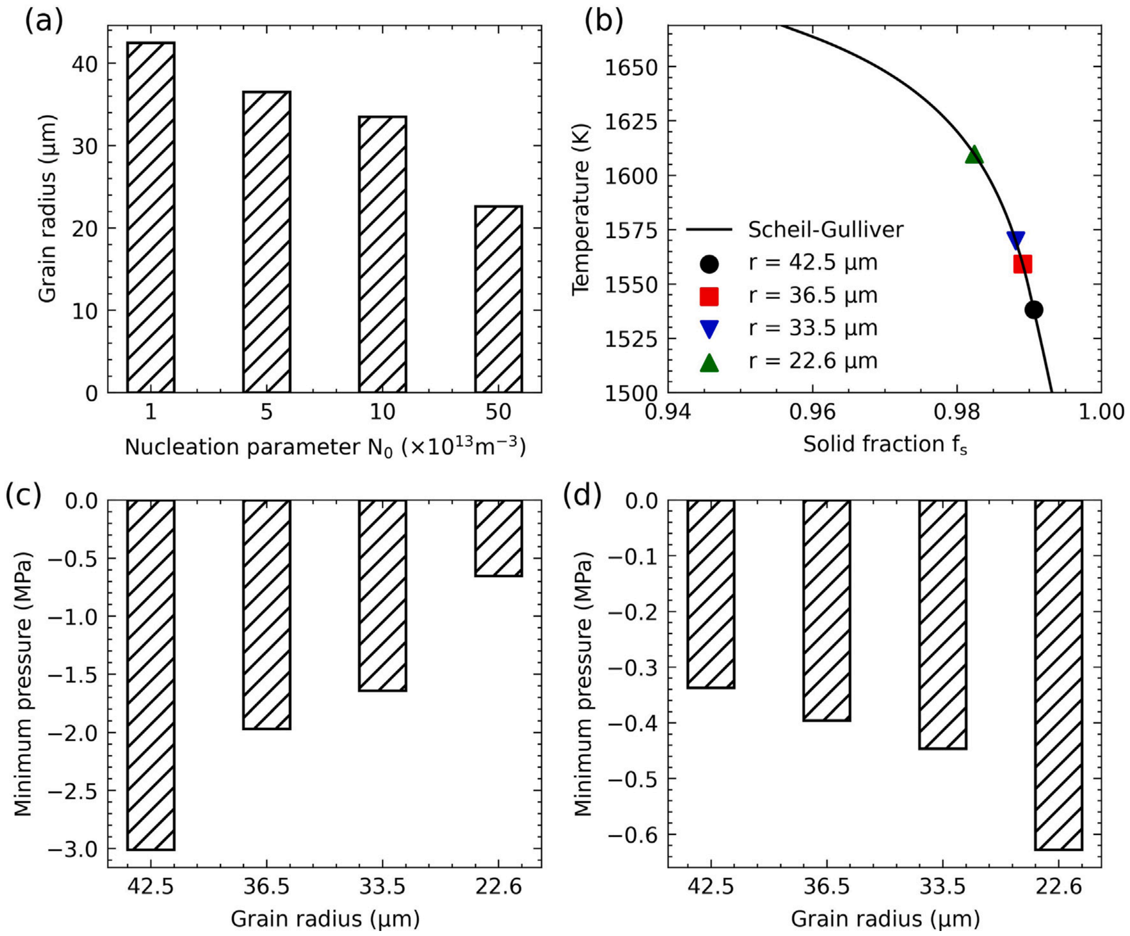

Fig. 10. The influence of the nucleation density on grain size of equiaxed grains and minimum pressure in the liquid channel network. (a) With increasing nucleation density n_0, the grain size of equiaxed grains decreases. (b) Scheil–Gulliver solidification curve of the TRIP steel. If a critical liquid channel width is used as the coalescence criterion, with decreasing grain size, the critical solid fraction decreases, while the coalescence temperature increases. (c) When a critical liquid channel width is used as the coalescence criterion, the maximum pressure drop decreases with decreasing grain size, indicating a reduction in SCS. (d) When a critical solid fraction is used as the coalescence criterion, the maximum pressure drop increases with decreasing grain size, representing a rise in SCS.

the field. Furthermore, the model's capability to evaluate solidification cracking susceptibility under diverse conditions makes it a practical tool for industrial applications.

However, it does have some limitations due to the assumptions made to simplify the problem. The pressure drop calculations, which are performed based on Eq. (17) [24,25], assume plane Poiseuille flow within liquid channels. This assumption is applicable for liquid channels between columnar grains but may introduce errors for liquid channels between equiaxed grains. Additionally, the separation velocity v_m in the pressure drop calculations is obtained by integrating the effective strain rate from the thermomechanical simulations under the assumption that solid does not deform in the mushy zone. This assumption might be invalid in regions with a large solid fraction, causing errors in the separation velocity v_m due to mechanical constraints. Moreover, the impact of liquid channel separation and fluid flow on deformation calculation in the thermomechanical analysis is not considered, as the thermomechanical model and the granular model is coupled sequentially, which may also cause errors in the calculated separation velocity v_m. Furthermore, the width of liquid channels is calculated based on the Scheil–Gulliver solidification curve and grain morphology. Compared to phase field simulations which solve the concentration profiles numerically, Scheil–Gulliver solidification calculation may overestimate segregation in the liquid channels [23], resulting in errors in the calculated liquid channel width. Addressing these issues would require a 3D full-field simulation of the whole mushy zone, which incorporates fluid dynamics, solid mechanics and solidification kinetics based on numerically solved concentration profiles. However, this approach requires significant computational resources, making it impractical at present.

5. Conclusions

In this work, a multi-scale multi-physics modeling framework has been developed to predict solidification cracking susceptibility (SCS) during welding. The modeling framework includes a thermo-mechanical model to simulate temperature and strain rate profile during welding, a cellular automata model to simulate solidified microstructure in the weld pool and a granular model to calculate pressure profile in the liquid channel network. The developed modeling framework is validated by comparing with welding experiments of TRIP steel and DP steel. The modeling framework is capable of capturing the influence of the process parameters, grain refinement and alloy composition on SCS. Thus, it provides a practical tool to evaluate SCS under various conditions.

For welding with a constant ratio between the power and the welding velocity, increasing welding velocity increases the length of the mushy zone, resulting in a drop in the minimum pressure in the liquid channel network and thus an increase in SCS. Meanwhile, increasing welding velocity promotes a columnar to equiaxed transition, which can inhibit solidification cracking for some alloys.

Grain refinement leads to a decrease in the separation velocities of the liquid channel interfaces and the permeability of the liquid channel network, favoring an increase in SCS. Meanwhile, it also increases the

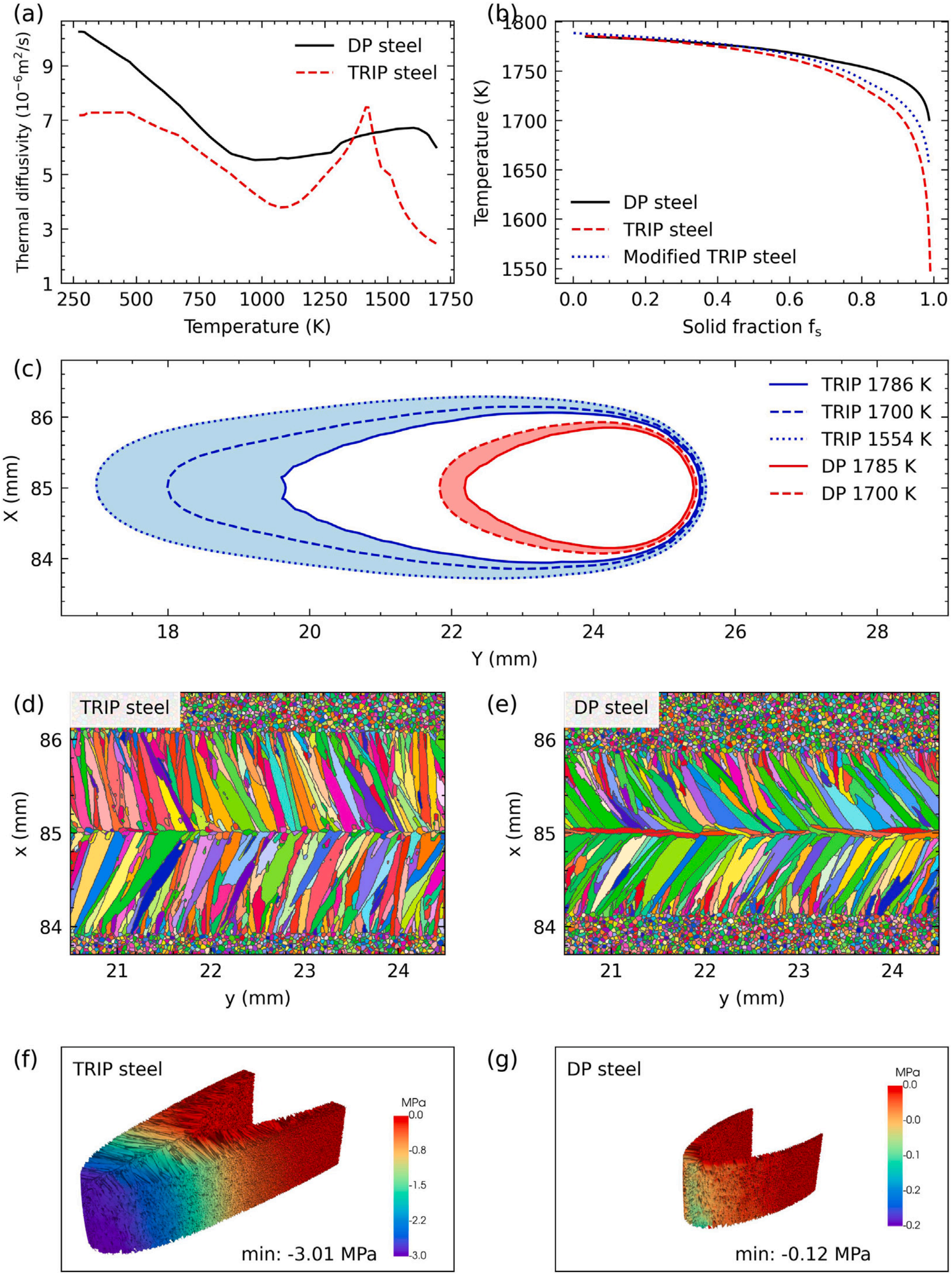

Fig. 11. Influence of the alloy composition on material properties, weld pool shape, solidified microstructure and solidification cracking susceptibility (SCS). (a) The thermal diffusivity of TRIP steel is smaller than that of DP steel across most of the temperature range of interest. (b) Scheil–Gulliver solidification curves of the TRIP steel and the DP steel, showing that TRIP steel has a larger freezing temperature range. (c) The melt pool and the mushy zone in the TRIP steel sample and the DP steel sample at welding velocity 10 mm/s. (d) and (e) The solidified microstructure in the TRIP steel sample and the DP steel sample, respectively. Grains are colored with IPF color with respect to Y direction. (f) and (g) The liquid pressure drop in the mushy zone of the TRIP steel sample and the DP steel sample. The absolute value of the minimum pressure in the DP steel sample (0.12 MPa) is much smaller than that in the TRIP steel sample (3.01 MPa). (For interpretation of the references to color in this figure legend, the reader is referred to the web version of this article.)

coalescence temperature of liquid channels, favoring a decrease in SCS. As a combined effect, SCS decreases by refining the microstructure.

Alloy composition has an impact on thermal diffusivity and segregation during solidification, which in turn influence SCS. Decreasing thermal diffusivity results in an elongated weld pool and mushy zone, consequently increasing SCS. With a stronger segregation, the freezing temperature range becomes larger, leading to a larger mushy zone and a larger SCS.

CRediT authorship contribution statement

Xiaohui Liang: Writing – review & editing, Writing – original draft, Software, Methodology, Conceptualization. **Gautam Agarwal:** Writing – review & editing, Methodology. **Marcel Hermans:** Writing – review & editing, Project administration. **Cornelis Bos:** Writing – review & editing, Project administration. **Ian Richardson:** Writing – review & editing, Project administration.

Declaration of competing interest

The authors declare that they have no known competing financial interests or personal relationships that could have appeared to influence the work reported in this paper.

Appendix A. Supplementary data

Supplementary material related to this article can be found online at https://doi.org/10.1016/j.actamat.2024.120530.

Data availability

The data generated in this study are available from the corresponding author upon request.

References

[1] S. Keeler, M. Kimchi, Advanced High-Strength Steels Application Guidelines V5, WorldAutoSteel, 2015.

[2] N. Coniglio, C. Cross, Effect of weld travel speed on solidification cracking behavior. Part 1: weld metal characteristics, Int. J. Adv. Manuf. Technol. 107 (2020) 5011–5023.

[3] N. Coniglio, C. Cross, Effect of weld travel speed on solidification cracking behavior. Part 2: testing conditions and metrics, Int. J. Adv. Manuf. Technol. 107 (2020) 5025–5038.

[4] A. Slyvinsky, H. Herold, M. Streitenberger, Influence of welding speed on the hot cracking resistance of the nickel-base alloy nicr25fealy during tig-welding, Hot Crack. Phenom. Welds (2005) 42–58.

[5] G. Goodwin, The effects of heat input and weld process on hot cracking in stainless steel, Weld. J. 67 (4) (1988) 88s–94s.

[6] G. Agarwal, H. Gao, M. Amirthalingam, M. Hermans, Study of solidification cracking susceptibility during laser welding in an advanced high strength automotive steel, Metals 8 (9) (2018) 673.

[7] S. Ohshita, N. Yurioka, N. Mori, T. Kimura, Prevention of solidification cracking in very low carbon steel welds, Weld. J. 62 (5) (1983) 129.

[8] M. Shibahara, H. Serizawa, H. Murakawa, Finite element method for hot cracking using temperature dependent interface element (report ii): Mechanical study of houldcroft test (mechanics, strength & structure design), Trans. JWRI 29 (1) (2000) 59–64.

[9] Suyitno V. Savran, L. Katgerman, D. Eskin, Effects of alloy composition and casting speed on structure formation and hot tearing during direct-chill casting of al-cu alloys, Metall. Mater. Trans. A 35 (2004) 3551–3561.

[10] E. Cicală, G. Duffet, H. Andrzejewski, D. Grevey, S. Ignat, Hot cracking in al–mg–si alloy laser welding–operating parameters and their effects, Mater. Sci. Eng. A 395 (1–2) (2005) 1–9.

[11] P. Schempp, C. Cross, A. Pittner, G. Oder, R.S. Neumann, H. Rooch, I. Dörfel, W. Österle, M. Rethmeier, Solidification of gta aluminum weld metal: Part 1—grain morphology dependent upon alloy composition and grain refiner content, Weld. J. 93 (2) (2014) 53s–59s.

[12] H. Gao, G. Agarwal, M. Amirthalingam, M. Hermans, I. Richardson, Investigation on hot cracking during laser welding by means of experimental and numerical methods, Weld. World 62 (2018) 71–78.

[13] T. Soysal, S. Kou, A simple test for assessing solidification cracking susceptibility and checking validity of susceptibility prediction, Acta Mater. 143 (2018) 181–197.

[14] N. Bakir, V. Pavlov, S. Zavjalov, S. Volvenko, A. Gumenyuk, M. Rethmeier, Development of a novel optical measurement technique to investigate the hot cracking susceptibility during laser beam welding, Weld. World 63 (2019) 435–441.

[15] M. Rappaz, J.M. Drezet, M. Gremaud, A new hot-tearing criterion, Metal. Mater. Trans. A 30 (1999) 449–455.

[16] S. Kou, A criterion for cracking during solidification, Acta Mater. 88 (2015) 366–374.

[17] J. Liu, S. Kou, Crack susceptibility of binary aluminum alloys during solidification, Acta Mater. 110 (2016) 84–94.

[18] T. Soysal, Effect of solidification models on predicting susceptibility of carbon steels to solidification cracking, Weld. World 65 (10) (2021) 1943–1954.

[19] C. Han, P. Jiang, S. Geng, S. Gao, G. Mi, C. Wang, Multiphase-field simulation of grain coalescence behavior and its effects on solidification cracking susceptibility during welding of al-cu alloys, Mater. Des. 211 (2021) 110146.

[20] L. Wang, N. Wang, N. Provatas, Liquid channel segregation and morphology and their relation with hot cracking susceptibility during columnar growth in binary alloys, Acta Mater. 126 (2017) 302–312.

[21] S. Geng, P. Jiang, X. Shao, G. Mi, H. Wu, Y. Ai, C. Wang, C. Han, R. Chen, W. Liu, et al., Effects of back-diffusion on solidification cracking susceptibility of al-mg alloys during welding: A phase-field study, Acta Mater. 160 (2018) 85–96.

[22] L. Yang, J. Yang, F. Han, Z. Zhang, Q. Li, Z. Dong, L. Wang, N. Ofori-Opoku, N. Provatas, Hot cracking susceptibility prediction from quantitative multi-phase field simulations with grain boundary effects, Acta Mater. 250 (2023) 118821.

[23] X. Liang, C. Bos, M. Hermans, I. Richardson, Influence of the temperature gradient and the pulling velocity on solidification cracking susceptibility during welding: A phase field study, Mater. Des. 235 (2023) 112424.

[24] M. Sistaninia, A. Phillion, J.-M. Drezet, M. Rappaz, Three-dimensional granular model of semi-solid metallic alloys undergoing solidification: Fluid flow and localization of feeding, Acta Mater. 60 (9) (2012) 3902–3911.

[25] M. Sistaninia, S. Terzi, A. Phillion, J.-M. Drezet, M. Rappaz, 3-d granular modeling and in situ x-ray tomographic imaging: A comparative study of hot tearing formation and semi-solid deformation in al–cu alloys, Acta Mater. 61 (10) (2013) 3831–3841.

[26] H.Z. Rajani, A. Phillion, A mesoscale solidification simulation of fusion welding in aluminum–magnesium–silicon alloys, Acta Mater. 77 (2014) 162–172.

[27] H.Z. Rajani, A. Phillion, 3-d multi-scale modeling of deformation within the weld mushy zone, Mater. Des. 94 (2016) 536–545.

[28] H.Z. Rajani, A. Phillion, 3D multi-scale multi-physics modelling of hot cracking in welding, Mater. Des. 144 (2018) 45–54.

[29] G. Agarwal, A. Kumar, I. Richardson, M. Hermans, Evaluation of solidification cracking susceptibility during laser welding in advanced high strength automotive steels, Mater. Des. 183 (2019) 108104.

[30] W. Kurz, B. Giovanola, R. Trivedi, Theory of microstructural development during rapid solidification, Acta Metall. 34 (5) (1986) 823–830.

[31] C.-A. Gandin, M. Rappaz, A 3d cellular automaton algorithm for the prediction of dendritic grain growth, Acta Mater. 45 (5) (1997) 2187–2195.

[32] X. Li, W. Tan, Numerical investigation of effects of nucleation mechanisms on grain structure in metal additive manufacturing, Comput. Mater. Sci. 153 (2018) 159–169.

[33] R. Shi, S.A. Khairallah, T.T. Roehling, T.W. Heo, J.T. McKeown, M.J. Matthews, Microstructural control in metal laser powder bed fusion additive manufacturing using laser beam shaping strategy, Acta Mater. 184 (2020) 284–305.

[34] L. Nastac, Numerical modeling of solidification morphologies and segregation patterns in cast dendritic alloys, Acta Mater. 47 (17) (1999) 4253–4262.

[35] M. Rappaz, A. Jacot, W.J. Boettinger, Last-stage solidification of alloys: Theoretical model of dendrite-arm and grain coalescence, Metall. Mater. Trans. A 34 (2003) 467–479.

[36] M. Opprecht, J.-P. Garandet, G. Roux, C. Flament, M. Soulier, A solution to the hot cracking problem for aluminium alloys manufactured by laser beam melting, Acta Mater. 197 (2020) 40–53.

[37] T. Nelson, J. Lippold, W. Lin, W. Baeslack III, Evaluation of the circular patch test for assessing weld solidification cracking, part i–development of a test method, Weld. J. 76 (3) (1997) 110–119.

[38] Z. Feng, T. Zacharia, S. David, On the thermomechanical conditions for weld metal solidification cracking, in: 77th Annual AWS Convention Abstracts, 1996, p. 1996.